LANGMUIR

pubs.acs.org/Langmuir Article

Unmasking the Hidden Threat: Conductive Under-Deposits and Their Role in Preferential Weldment Corrosion of Carbon Steel under Sour Conditions

Adewale K. Ipadeola,* Mostafa H. Sliem, Dana Abdeen, Nicholas Laycock, Ashwin RajKumar, Phaneendra K. Yalavarthy,* and Aboubakr M. Abdullah*

Cite This: *Langmuir* 2025, 41, 23632−23651 Read Online

ACCESS | Metrics & More | Article Recommendations | Supporting Information

ABSTRACT: This work incorporates precorrosion conditioning and conductive deposits (FeS or FeS_2) to explore corrosion mechanisms across base metal (BM), weld metal (WM), and heat-affected zone (HAZ) regions under simulated sour conditions (NaCl (3.5 wt %), $Na_2S_2O_3$ (1000 ppm), CH_3COOH (100 ppm), CO_2, 60 °C, pH ∼ 4, and 1000 rpm). Electrochemical studies demonstrated various corrosion rates (CR) hierarchies (CS-BM (0.34−0.42 mmpy) < CS-WM (0.38−0.73 mmpy) < CS-HAZ (0.48−1.75 mmpy)), which were exacerbated by FeS or FeS_2 deposition. This was ascribed to a variety of potential variations and localized acidification. Also, there were notable changes in the welded CS areas' compositions and microstructures both before and after corrosion testing. By creating protective layers that reduce microgalvanic interactions, the commercial amine-based inhibitor CRW11 (200 ppm) showed remarkable potency by lowering the CRs (<0.1 mmpy) threshold with inhibition efficiency (IE = >80%). Corrosion products (α-$Fe^{3}O_3$, γ-FeOOH, and Fe_3O_4) were most significant, identified by Raman spectroscopy. 1D artificial pit tests showed varied pit propagation dynamics, especially under FeS-induced heterogeneity, with CS-BM-FeS having the highest pit depth (71.4 ± 11.8 μm), but increased pit density (568.0 mm^2) was recorded for CS-HAZ-FeS_2. This proves the impact of conductive deposits on the pitting of welded CS regions. These findings corroborated deposit-induced electrochemical heterogeneity with localized attack, which was most significant with FeS_2 deposit. Machine learning (ML) models, like random forest (RF), decision tree (DT), and extreme gradient boost (XGBoost), demonstrated excellent IE predictive ability (R^2 = 0.99) for welded CS without/with conductive deposits. However, RF and XGBoost are ideal with the least RMSE/MAE (0.2/0.2 and 0.1/0.1) for welded CS without/with FeS and FeS_2, respectively. These results provide a practical foundation for pitting and PWC in preconditioned welded CS with conductive deposits, allowing for the best material selection and corrosion control techniques in sour service applications.

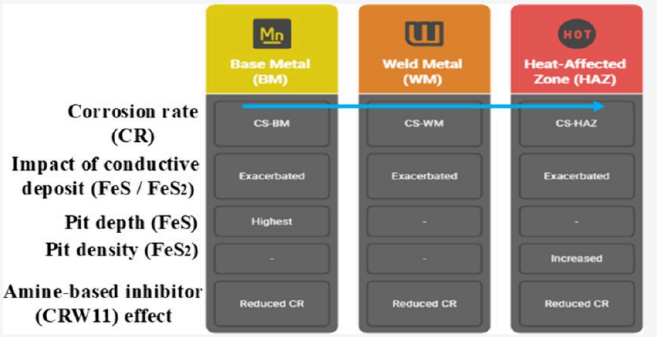

Downloaded via INDIAN INST OF SCIENCE on September 14, 2025 at 08:22:37 (UTC).
See https://pubs.acs.org/sharingguidelines for options on how to legitimately share published articles.

1. INTRODUCTION

Preferential weldment corrosion (PWC) and pitting corrosion in sour environments pose significant integrity challenges for welded X65 carbon steel (CS) pipelines in oil and gas systems.[1] These corrosion mechanisms are driven by complex interactions between microstructural heterogeneity, compositional variations, environmental conditions, and operational parameters.[2] PWC arises from galvanic potential differences between the regions of welded CS, i.e., base metal (BM), weld metal (WM), and heat-affected zone (HAZ), with distinct compositional and microstructural profiles created during welding processes.[3] In sour service environments (i.e., H_2S and CO_2), these are worsened by conductive iron sulfide deposits (FeS and FeS_2) that promote localized acidification and microgalvanic coupling.[4] For instance, Nesic and co-workers[5] proved that FeS films could act as both protective barriers and catalysts for corrosion, depending on their morphology and stability. However, Rebak and Perez showed that FeS_2 deposits were particularly detrimental, creating persistent acidic microenvironments that accelerate pitting initiation.[6] The complexity of PWC and pitting in sour environments is further raised by the dynamic nature of operational conditions in oil and gas pipelines. Fluctuations in flow rates, temperatures, and chemical compositions can lead to cyclic periods of active corrosion and partial protection,[7] creating metastable interfaces that are challenging to model

Received: May 29, 2025
Revised: August 18, 2025
Accepted: August 18, 2025
Published: August 27, 2025

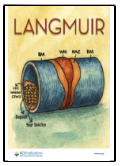

ACS Publications © 2025 American Chemical Society

https://doi.org/10.1021/acs.langmuir.5c02733
Langmuir 2025, 41, 23632−23651

prediction. For example, a study revealed how turbulent flow conditions stripped protective scales and exposed reactive weldment interfaces,[6] while another study confirmed the impact of temperature cycling on the stability of corrosion product films.[8] These studies underscore the need for a comprehensive understanding of corrosion mechanisms under realistic and dynamic conditions in the oil and gas facilities.

Corrosion inhibitors are widely deployed as a mitigation strategy, but their effectiveness becomes unpredictable under complex environmental conditions and conductive deposits.[9] Papavinasam and co-workers[10] showed that some inhibitor formulations could unexpectedly accelerate WM/HAZ attack through selective film disruption. The interaction between inhibitors and weldment regions was further complicated by preferential adsorption behaviors, as proved by Liu et al.[11] They found that amine-based inhibitors show reduced efficacy on HAZ compared to BM, due to differences in surface energy and microstructure. The complexities stem from variable adsorption behaviors, environmental factors, and metallurgical differences between BM, WM, and HAZ. Corrosion inhibitors face reduced reliability in systems with deposits (e.g., FeS, FeS_2, salts, organic acids) or fluctuating conditions (temperature, pH). For example, amine-based inhibitors were reported to have reduced adsorption capacity and led to escalating corrosion rates in CO_2-rich environments with acetic acid.[12] This aligns with the observation that acidic species disrupt protective films through competitive adsorption.[13] For instance, α-aminophosphonate inhibitors revealed peak efficacy inhibition (92−95%) at 180 ppm in HCl/H_2SO_4 environments, but efficiency dropped sharply at lower concentrations. This nonlinear response highlights sensitivity to dosage in dynamic systems. Also, these inhibitors' efficacy on CS was lost at 60 °C, owing to molecular degradation.[14]

Recent studies have elucidated the significant impact of precorrosion surface conditions and conductive deposit morphology on the initiation and propagation of corrosion processes and pitting.[15] Sophisticated surface characterization techniques revealed how pre-existing corrosion products influenced the nucleation and growth of iron sulfide (FeS) and iron disulfide (FeS_2) deposits.[16] This resulted in the formation of localized electrochemical cells with enhanced cathodic activity. Also, the finding showed the complex interplay between surface chemistry, microstructure, and environmental factors in corrosion mechanisms. However, a comprehensive mechanistic understanding remains elusive due to the insufficient integration of electrochemical, microstructural, environmental variables, and machine learning (ML) models in current research paradigms.[17] This knowledge gap is particularly obvious for welded joints of CS exposed to sour service conditions, where alternating periods of active corrosion and inhibitor protection create complex metastable interfaces.[18] The dynamic nature of the systems presents significant challenges in predicting and mitigating corrosion phenomena in industrial applications.[19]

Conventional corrosion prediction models exhibit fundamental limitations in addressing the multivariate interdependencies among weldment microstructure, inhibitor adsorption kinetics, and conductive deposits. While linear regression and empirical formulations provide first-order approximations of corrosion behavior, their reliance on simplified assumptions prevents accurate quantification of nonlinear dose−response relationships or synergistic effects arising from complex interfacial phenomena.[20,21] The ML algorithms have transformed corrosion modeling and inhibitor optimization by effectively handling high-dimensional parameter spaces and capturing emergent system behavior. For instance, multilayer perceptrons (MLPs) revealed exceptional predictive performance ($R^2 > 0.95$) for CO_2-induced corrosion through hierarchical feature abstraction of environmental variables.[22,23] In soil-buried steel systems, random forest (RF) regressors showed superior accuracy (RMSE = 0.01095 A/m^2) for corrosion current density predictions.[22] This was attributed to the ensemble approach of evaluating split improvements across numerous decision trees. Neural networks have excelled in optimizing inhibitor formulations by employing gradient-based learning on chemical descriptor matrices.[24] This enabled simultaneous maximization of adsorption energy and charge transfer resistance. Notably, RF and decision tree (DT) algorithms were successfully applied to optimize corrosion inhibitor formulations for specific operational conditions,[25] leveraging the model's ability to capture complex interactions between inhibitor components and environmental factors. The ML algorithms represent a significant leap forward in corrosion science, providing powerful tools for predicting CRs, inhibition efficiency (IE), inhibition power and developing tailored protective strategies across diverse environmental conditions and material systems.[26]

This work investigates advances in the field of corrosion science through a comprehensive multitechnique approach combining electrochemical analysis, surface characterization, and machine learning to elucidate corrosion mechanisms in preconditioned X65 welded CS without/with FeS and FeS_2 deposits. By simulating realistic sour service environments, this study provides critical insights into localized attack propagation and amine-based corrosion inhibitor (denoted as CRW11) performance without/with conductive deposits. The integration of artificial pit growth with one-dimensional (1D) artificial pit technique and Raman spectroscopy mapping addresses longstanding knowledge gaps about pitting and corrosion product evolution, respectively. Also, the development of predictive ML algorithms incorporating all input parameter descriptors represents a paradigm shift in corrosion management strategies, enabling proactive risk assessment for welded infrastructure under complex operating conditions. This comprehensive approach builds upon and extends the work of pioneers in the field, such as Kermani and Morshed,[27] who laid the foundation for understanding sour corrosion mechanisms, and other contributions on the electrochemical behavior of welded joints in H_2S-containing environments.[28] The experimental methodologies, integration of advanced analytical techniques, and ML models adopted in this study provide a more nuanced understanding of corrosion processes in complex industrial environments, particularly in the welded CS pipelines, potentially leading to improved corrosion mitigation strategies and enhanced infrastructure longevity. Besides streamlining the inspection protocols, including regular corrosion rate, integrity monitoring, frequent/specific nondestructive testing (NDT), chemical/mechanical feature verification, and conformity to NACE standards.

2. MATERIALS AND EXPERIMENTAL PROCEDURE

2.1. Materials and Reagents. Analytical grade chemicals were sourced from Sigma-Aldrich (St. Louis, MO, USA), including NaCl, $Na_2S_2O_3$, C_3H_7OH, $(CH_3)_2CO$, CH_3COOH, Nafion solution, and CO_2 gas. Milli-Q water, and polishing pads. Laboratory conductive deposits with mesh sizes (FeS (140 nm) and FeS_2 (44 nm)) having

https://doi.org/10.1021/acs.langmuir.5c02733
Langmuir 2025, 41, 23632−23651

similar morphology and porosity to field deposit were also used. X65 welded CS pipeline was provided by Qatar Shell. Commercial amine-based corrosion (CRW11l) inhibitor was obtained from Baker Hughes. The X65 welded CS regions were further machined into base metal (BM), welding metal (WM), and heat-affected zone (HAZ), whose elemental compositions obtained from XRF and EDX are summarized in Table 1.

Table 1. Elemental compositions of X65 welded CS regions (BM, WM, and HAZ), from XRF and EDX analysis, before corrosion tests

	XRF (wt %)			EDX (wt %)		
elemental compositions	BM	WM	HAZ	BM	WM	HAZ
C	-	-	-	2.2	2.4	2.4
Fe	97.8	97.6	97.8	91.9	89.9	90.9
Al	0.3	0.2	0.3	0.2	0.2	0.2
Si	0.1	0.2	0.1	0.7	0.3	0.7
Ca	0.1	-	0.1	-	-	-
Cr	0.3	0.04	0.3	0.5	0.2	0.6
Mn	1.1	0.9	1.1	1.7	2.0	0.9
Nb	0.02	-	0.02	-	-	-
Mo	0.2	0.2	0.2	0.2	-	-
Sc	-	0.03	-	-	-	-
Ni	-	0.7	-	-	1.0	-
Zn	-	-	-	-	1.4	-
P	-	0.01	-	-	-	-

2.2. X65 Carbon Steel Coupon Machining, Polishing, and Preconditioning Method. Cylindrical specimens (5 × 60 mm) were machined from the WM, HAZ, and BM regions of an X65 grade welded CS pipeline (Figure 1a), perpendicular to the pipeline axis

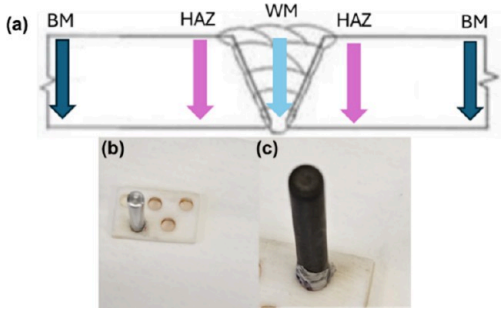

Figure 1. (a) Area and direction of cutting WM, HAZ, and BM, (b) polished X65 carbon steel, and (c) preconditioned X65 carbon steel in sweet media.

(marked with arrows). Samples were polished to a mirror finish using progressively finer grits (220−2000). The coupons were then cleaned with deionized water and isopropanol before storage in a controlled environment (Figure 1b). A 1.0 wt % NaCl solution was deoxygenated with N_2 gas for 2 h under stirring. The polished CS rods were then placed in an autoclave with a deoxygenated solution, purging with CO_2 at 40 psi and 50 °C for 1.5 h. This process formed a uniform, greyish protective scale on X65 welded CS coupons (Figure 1c). This condition favored iron oxide scale formation over iron carbonate ($FeCO_3$) because of the stability of iron oxides in the presence of chloride ions. Corrosion analysis was conducted immediately after this preconditioning.

2.3. Deposit Ink Preparation. Synthetic pipeline conductive deposits were simulated in the laboratory. FeS and FeS_2 (300 mg each) were suspended in a mixture of isopropyl alcohol and Nafion, then sonicated. The suspensions were deposited on X65 welded CS rod substrates and dried in two stages: air-drying (2 h) and oven treatment (80 °C for 4 h). This process created an adherent deposit covering 75% of the substrate surface, mimicking real pipeline deposits.

2.4. Sample and Electrolyte Preparation for Corrosion Tests. X65 welded CS samples machined from WM, HAZ, and BM regions were tested for corrosion studies in sour media. The samples were encapsulated in epoxy resin, exposing 0.2 cm^2 of surface area, then degreased, rinsed, and preconditioned. Electrochemical tests were conducted in a simulated sour environment, i.e., NaCl (3.5 wt %), $Na_2S_2O_3$ (1000 ppm), and CH_3COOH (100 ppm), under CO_2 purging at 60 °C, pH ∼ 4, and 1000 rpm. $Na_2S_2O_3$ and CH_3COOH substituted H_2S for safety reason. This setup allows precise control of environmental parameters, mimicking field operational pipeline conditions for corrosion and inhibitor efficacy studies.

The commercial amine-based corrosion inhibitor, CRONOX-CRW85711, abbreviated as CRW11, was used at 200 ppm concentration in a glycol-aqueous solution. Specimens were mounted on a rotating electrode assembly spinning at 1000 rpm to simulate flow conditions.

2.5. Electrochemical Measurements. Electrochemical corrosion measurements were conducted using a GAMRY 3000 potentiostat, employing open circuit potential (OCP), electrochemical impedance spectroscopy (EIS), and linear polarization potential (LPR) techniques. The setup included a three-electrode double-jacketed cell with temperature control. An X65 welded CS rod served as the working electrode, Ag/AgCl saturated KCl as the reference electrode, and a graphite rod as the counter electrode. Experiments were performed under simulated sour conditions (NaCl (3.5 wt %), $Na_2S_2O_3$ (1000 ppm), CH_3COOH (100 ppm), CO_2 saturation, 60 °C, 1000 rpm, and pH ∼ 4). EIS analysis was conducted from 0.1 Hz to 100 kHz with 10 mV AC amplitude, followed by LPR measurements. All tests were performed in triplicate to ensure reproducibility and adherence to industrial standards for evaluating materials in sour service environments. EIS data were fitted using Voigt electrical equivalent circuits (EECs), while LPR data were processed to calculate corrosion current (i_{corr}), CRs, and IE, using eqs i−iii.

$$\text{Corrosion current } (i_{corr},\ \text{mA/cm}^2) = \left(\frac{B}{R_{ct}}\right) \times 1000 \quad \text{(i)}$$

where B is the stern constant, which is equal to 0.026 V, and R_p (R_{ct}) is the charge transfer/polarization resistance in Ω·cm^2.

$$\text{Corrosion rate (CR, mmpy)} = \frac{i_{corr} \times 10 \times M \times 3.15 \times 10^7}{\rho \times n} \quad \text{(ii)}$$

where CR is the corrosion rate (mmpy), i_{corr} is the corrosion current in mA/cm^2, M is the molar mass of iron (Fe), which is equal to 55.85 g/mol, ρ its volume density (7.87 g/cm^3), and n = number of electrons (2).

$$\text{Inhibition efficiency (IE)} = \left(\frac{i_{\text{CS no inhibitor}} - i_{\text{CS with inhibitor}}}{i_{\text{CS no inhibitor}}}\right) \times 100 \quad \text{(iii)}$$

where $i_{cs\ with\ inhibitor}$ and $i_{no\ inhibitor}$ are the current densities of the inhibited and bare carbon steel, respectively.

2.6. Weight Loss Measurements for Base Metal. The weight loss study was performed on static carbon steel samples (15 × 15 × 1 mm) in a sour electrolyte. Samples were polished, preconditioned in N_2 purged 1 wt % NaCl, then exposed to CO_2 at 40 psi and 50 °C. They were immersed in a CO_2-saturated 3 wt % NaCl solution with $Na_2S_2O_3$ and acetate at 60 °C, without/with the CRW11 inhibitor (Figures 2a,b). Duplicate samples were removed at 144, 336, and 500 h, cleaned with ammonium citrate (20 wt %, Figures 2c,d), dried, and weighed. The CRs were calculated from average weight loss measurements and calculated using eqs iv and v.

$$\text{Corrosion rate (CR, mpy)} = \frac{534 \times W}{\rho \times A \times t} \quad \text{(iv)}$$

https://doi.org/10.1021/acs.langmuir.5c02733
Langmuir 2025, 41, 23632−23651

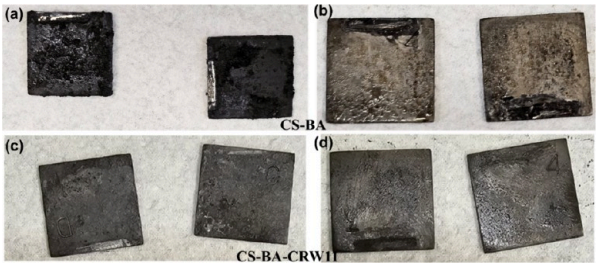

Figure 2. Images of X65 CS coupons after weight loss corrosion test (a) CS-BM, (b) CS-BM-CRW11 before washing with ammonium citrate solution, and (c) CS-BM and (d) CS-BM-CRW11 after washing with ammonium citrate solution.

$$\text{But CR, mmpy} = \text{CR(mpy)} \times 0.0254 \quad \text{(v)}$$

W (weight loss (final − initial weights)), ρ (density of C-steel (7.84 g)), A (area of samples exposed (2.25 cm^2)), immersion time (144, 336, and 500 h).

2.7. 1D Pit Techniques. 1D artificial pit electrodes were created using 1000 μm diameter welded CS wires (CS-BM, CS-WM, and CS-HAZ) embedded in epoxy resin. A custom 3D-printed mold facilitated the creation of a multielectrode array, allowing simultaneous testing of electrodes without and with conductive deposits (FeS and FeS_2) (Figure 3a). The vertical array was immersed in simulated sour electrolyte with a hot water bath circulator to maintain the temperature (60 °C) and connected to the potentiostat to study pit formation. This method enables investigation of localized corrosion in welded CS structures under controlled conditions. The welded CS specimen was prepared by wet abrasion to a 2000-grit finish and then vertically inverted and uniformly exposed to the simulated sour electrolyte at 60 °C (Figure 3b). To improve pit depth measurement accuracy, vacuum was applied during resin curing to eliminate microbubbles, and wires were thoroughly cleaned to prevent crevice formation and contamination. These steps enhanced the experimental setup's reliability.

The deposition process on wire electrodes mirrored that used for planar electrodes, utilizing plastic cups and mesh covers to encase the wire cross-section. Electrochemical characterization, including chronoamperometry (CA), OCP, and EIS, was performed without and with deposits over the artificial pit cavity. The setup used a sour electrolyte solution with electrodes as anodes at 60 °C. This method allowed for the measurement of key parameters such as pit depth (d_{pit}), pit area, pit density, aspect ratio, pit resistance, pit current density, and pit propagation rates for different welded regions (CS-BM, CS-WM, CS-HAZ) without/with various deposits (FeS and FeS_2) in simulated sour conditions. Pit depth was calculated using Faraday's second law of electrolysis, given in eq vi.

$$d_{pit} = \frac{QM_w}{A \cdot \rho \cdot n \cdot F} \quad \text{(vi)}$$

Q represents charge (current × time), A is the wire's cross-sectional area (0.0079 cm^2), d_{pit} is pit depth, ρ is iron's density (7.85 g/cm^3), n is the assumed average ion charge during dissolution (2), F is Faraday's constant (96485 C/mol), and M_w is iron's atomic weight (55.845 g/mol).

2.8. Surface Morphology and Characterization. The X65 carbon steel coupons from different areas (BM, WM, and HAZ) were analyzed using advanced characterization techniques. Scanning electron microscopy (SEM) coupled with elemental dispersive X-ray spectroscopy (EDX) was employed to examine surface morphologies, elemental compositions, and mapping before and after corrosion tests. X-ray fluorescence (XRF) was used to determine bulk metal contents, while optical microscopy revealed microstructures. Raman spectroscopy was utilized to analyze corrosion products on welded coupons in the presence of inhibitors, without deposits, under sour conditions.

2.9. Data Set Construction and Machine Learning Model Development. The data set integrates measurements from EIS and LPR techniques, creating a robust foundation for ML model training. It incorporates key variables such as electrochemical method, deposit types (FeS and FeS_2), and corrosion inhibitor (CRW11). Categorical variables were one-hot encoded for ML compatibility. The final data set comprises 144 evenly distributed data points across electrochemical techniques.

The data set was partitioned into input features and a single output target: inhibitor efficiency (IE). Input features include electrochemical methodology, deposit formation, the CRW11 inhibitor, and measurements from EIS and LPR techniques. This division enabled the development and assessment of the predictive models that explore relationships between diverse inputs and predicted inhibitor efficiency. The data set was split using 80/20 stratified sampling for training and testing. This preserved the distribution of electrochemical methodologies across both subsets, ensuring representative sampling and reducing bias. The approach allows for robust evaluation of the ML model's performance and generalizability across diverse electrochemical data.

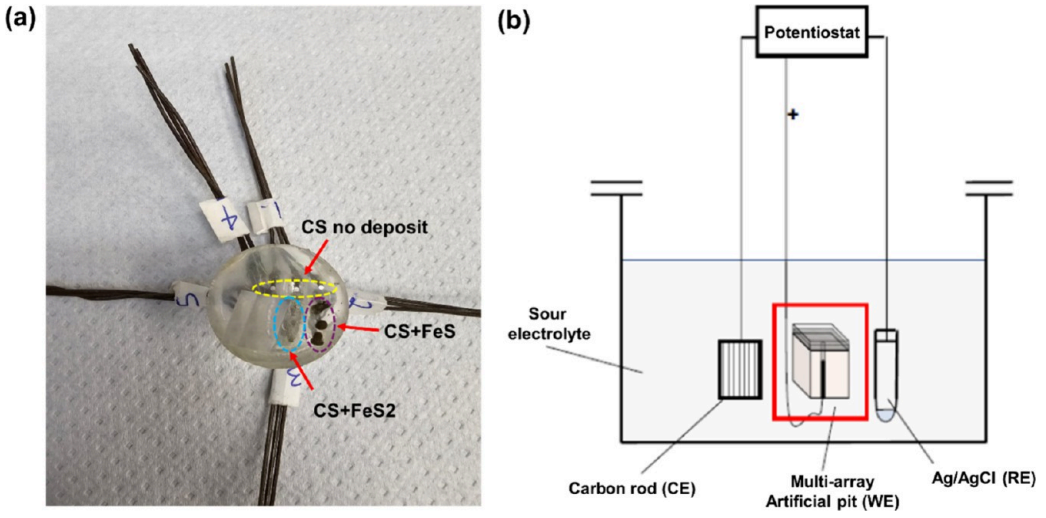

Figure 3. 1D artificial pit technique setup (a) a 1000 μm diameter wires embedded in transparent epoxy with a plastic cup fixed at the pit mouth with/without FeS or FeS_2 deposits, and (b) vertically inverted 1D multiple electrodes in sour electrolyte connected to the potentiostat for the formation of an artificial cavity.

https://doi.org/10.1021/acs.langmuir.5c02733
Langmuir 2025, 41, 23632−23651

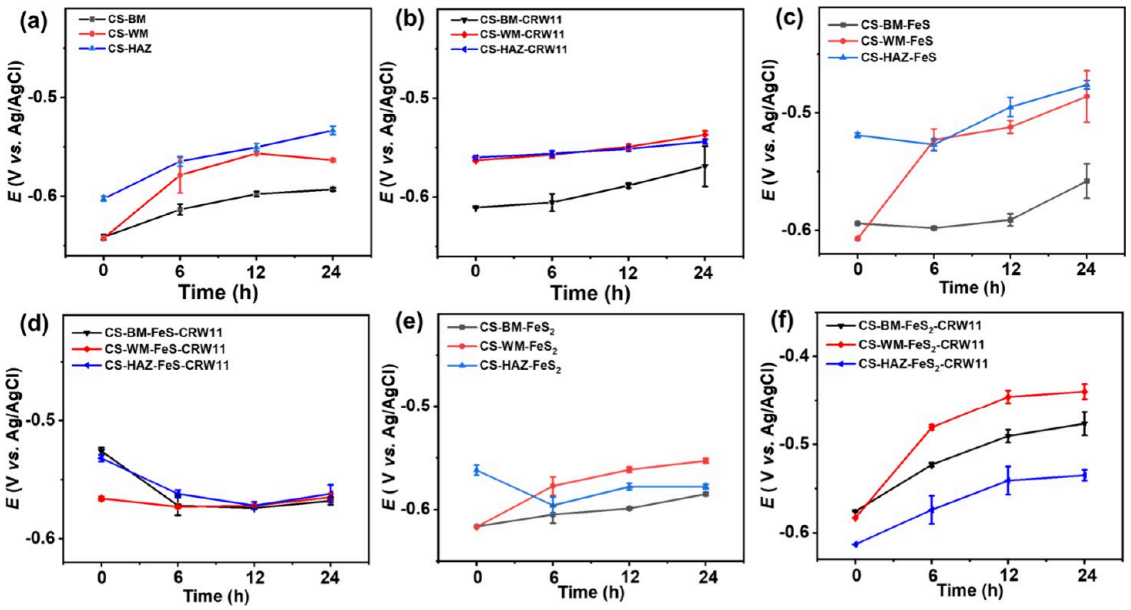

Figure 4. OCP with preconditioning before corrosion in simulated sour conditions of (a) welded CS, (b) welded CS + CRW11, (c) welded CS + FeS, (d) welded CS + FeS + CRW11, (e) welded CS + FeS_2, and (f) welded CS + FeS_2 + CRW11.

We evaluated seven regression algorithms: linear regression (LR), support vector regressor (SVR), k-nearest neighbors (KNN) regression, random forest (RF), decision tree (DT), gradient boosting (GB), and extreme gradient boosting (XGBoost) to predict inhibition efficiency in a data set with mixed variable types. These algorithms were chosen due to their robustness to overfitting, ability to handle nonlinear relationships, and suitability for data sets with mixed categorical and continuous variables. Specifically, RF and DT offer transparent interpretability through feature importance ranking, while XGBoost is known for its high predictive performance in complex regression tasks. Performance was assessed using coefficient of determination (R^2), root-mean-square error (RMSE) and mean absolute error (MAE) metrics. To ensure robust generalization and mitigate overfitting, we implemented a 4-fold cross-validation strategy.[29] This approach provided a comprehensive evaluation of each algorithm's predictive capabilities across different data partitions.

3. RESULTS AND DISCUSSION

3.1. Corrosion Measurements. The experiments detailed in this section were conducted under controlled preconditioning protocols applied to the welded CS coupons prior to corrosion testing. These tests were performed without/with conductive deposits (FeS and FeS_2), and in the absence/presence of the CRW11 inhibitor under simulated sour conditions.

3.1.1. Open Circuit Potential. At the start of exposure, CS-BM and CS-WM showed lower open circuit potential (E_{OCP}) than CS-HAZ in a simulated sour environment. Initially, CS-BM and CS-WM were cathodic, while CS-HAZ was anodic. Over time, the E_{OCP} of CS-WM converged with that of CS-HAZ, both becoming anodic, while CS-BM remained cathodic (Figure 4a). This suggests that, in comparison to CS-WM and CS-BM, CS-HAZ is more likely to corrode in sour environments, but at longer exposure times. CS-HAZ and CS-WM are both more susceptible to corrosion. Addition of the CRW11 inhibitor did not significantly alter these galvanic relationships (Figure 4b). These observations reveal potential differences (<150 mV) in CS under sour conditions, with or without the inhibitor, due to heterogeneous microstructures and compositions.[30,31] The persistence of potential differences, even with CRW11 inhibitor addition, underscores the significant impact of welding-induced microstructural variations on the electrochemical behavior of the material. This highlights the need for targeted corrosion mitigation strategies in complex systems.

FeS deposits ($^3/_4$ coverage) initially made CS-BM-FeS and CS-WM-FeS cathodic, while CS-HAZ-FeS became anodic (Figure 4c). Over time, CS-WM-FeS shifted to anodic behavior, joining CS-HAZ-FeS, while CS-BM-FeS remained cathodic. This suggests that CS-HAZ-FeS was the most prone to corrosion, among other locations. Long-term exposure, however, changed this arrangement, making the CS-HAZ-FeS and CS-WM-FeS more vulnerable to sour corrosion. The CRW11 inhibitor reversed these roles, making CS-BM-FeS-CRW11 and CS-HAZ-FeS-CRW11 anodic and CS-WM-FeS-CRW11 cathodic (Figure 4d). CRW11 effectively reduced potential differences among welded CS components in FeS-rich sour conditions, without causing galvanic coupling. These results clarify the impact of FeS deposits on welded CS in sour environments, with and without the CRW11 inhibitor.

The preconditioned welded CS with FeS_2 deposits revealed distinct electrochemical interactions between CS-BM, CS-WM, and CS-HAZ. Initially, CS-BM-FeS_2 and CS-WM-FeS_2 were cathodic, while CS-HAZ-FeS_2 was anodic. After 24 h, polarity reversed, with CS-WM-FeS_2 becoming anodic (Figure 4e). This implies that CS-HAZ-FeS_2 is initially more likely to corrode in sour environments than CS-WM and CS-BM, but that CS-WM-FeS_2 is more prone to rust at longer exposure times. Introduction of the CRW11 inhibitor altered these relationships, initially making CS-BM-FeS_2-CRW11 and CS-WM-FeS_2-CRW11 anodic and CS-HAZ-FeS_2-CRW11 cathodic (Figure 4f). Over time, CS-BM-FeS_2-CRW11 stabilized at an intermediate potential between cathodic CS-HAZ-FeS_2-CRW11 and anodic CS-WM-FeS_2-CRW11. The inhibitor effectively reconfigured the varied potential differences, establishing CS-WM-FeS_2-CRW11 and CS-BM-FeS_2-CRW11 as persistent anodic sites, while CS-HAZ-FeS_2-CRW11 maintained cathodic dominance. These findings elucidate FeS_2-mediated corrosion dynamics in welded CS systems

https://doi.org/10.1021/acs.langmuir.5c02733
Langmuir 2025, 41, 23632−23651

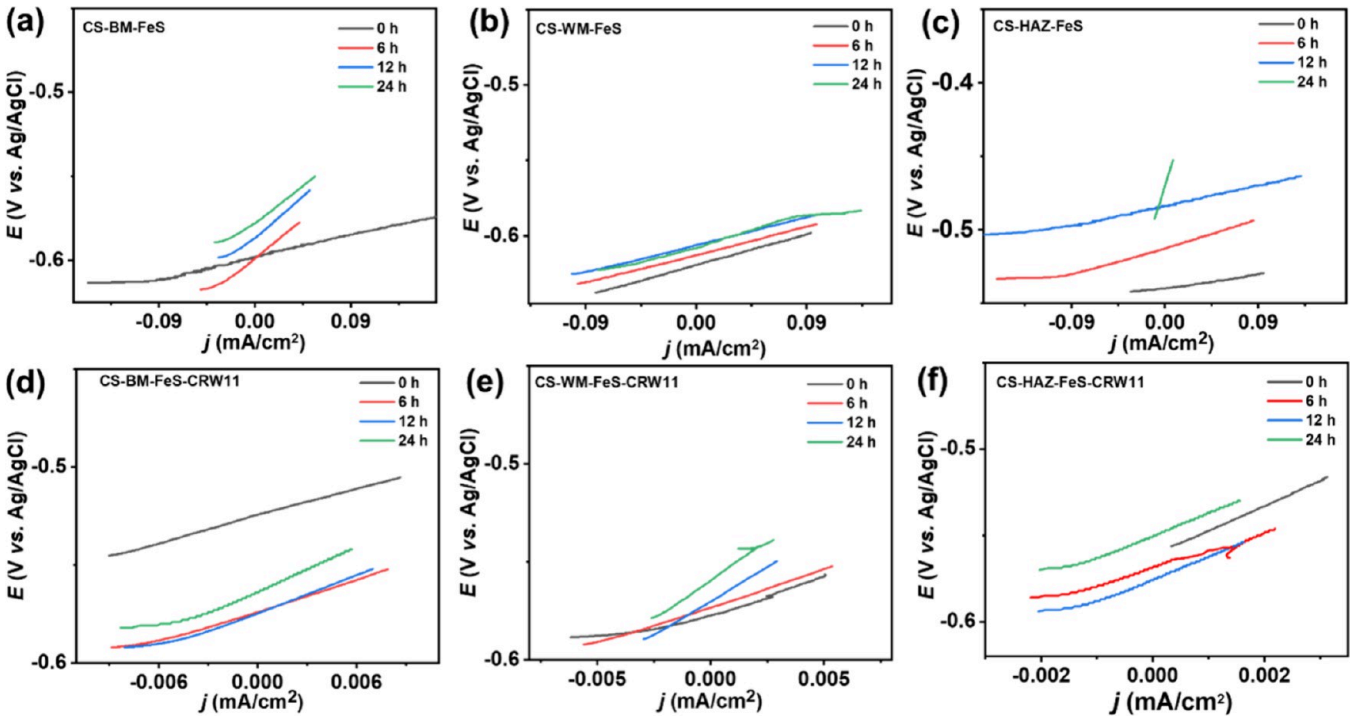

Figure 5. LPR with preconditioning before corrosion in simulated sour conditions of (a) CS-BM-FeS, (b) CS-WM-FeS, (c) CS-HAZ-FeS, (d) CS-BM-FeS-CRW11, (e) CS-WM-FeS-CRW11, and (f) CS-HAZFeS-CRW11.

and demonstrate CRW11's ability to modify potential differences, although not sufficiently to cause significant galvanic interactions under sour conditions. Notably, all localized corrosion experiments show modest OCP fluctuations (indicated by error bars) because of the constant changes in the metal's surface conditions, such as surface inhomogeneities, film formation/breakdown, pitting, and environmental instabilities.[32]

3.1.2. Linear Polarization Potential. The CRs of welded CS samples were evaluated in simulated sour conditions using LPR. Without the CRW11 inhibitor, CRs increased over time, with CS-HAZ showing the highest CR values, followed by CS-WM and CS-BM (Figure S1a−c). The introduction of the CRW11 inhibitor significantly reduced the CRs, significantly bringing them below the 0.1 mmpy industry standard (Figures S1d−f). However, CS-WM-CRW11 and CS-BM-CRW11 initially showed higher CRs with the inhibitor, suggesting that CRW11 needs more time to achieve optimal coverage on these regions, possibly due to their microstructural characteristics, i.e., larger and coarser grain boundaries. This observation is consistent with previous reports.[33,34] The observed time-dependent efficacy of CRW11 across different welded CS regions underscores the significant impact of microstructural variations on inhibitor performance in simulated sour media.

Also, coverage of FeS deposit (75%) on welded CS under simulated sour conditions was examined. Without inhibitor, CRs fluctuated, with CS-WM-FeS showing the highest CRs, followed by CS-BM-FeS and CS-HAZ-FeS (Figures 5a−c). The addition of the CRW11 inhibitor significantly reduced the CRs below 0.1 mmpy over time, though CS-WM-FeS and CS-BM-FeS initially showed slightly higher CRs (Figures 5d−f). The inhibited CR trend was CS-HAZ-FeS-CRW11 < CS-WM-FeS-CRW11 < CS-BM-FeS-CRW11. This suggests that CRW11 requires more time to achieve optimal coverage and reactivity on CS-WM-FeS and CS-BM-FeS, possibly due to their larger grain boundaries and FeS_2 deposit effect.

The corrosion behavior of welded CS samples partially covered with FeS_2 deposit was studied under simulated sour conditions. Without the CRW11 inhibitor, CRs fluctuated, with CS-WM-FeS_2 showing the highest CRs (0.56−1.01 mmpy), followed by CS-BM-FeS_2 and CS-HAZ-FeS_2 (Figures S2a−c). The addition of CRW11 significantly reduced CRs below 0.1 mmpy for all samples, with CS-HAZ-FeS_2-CRW11 exhibiting the lowest CRs (0.05−0.07 mmpy), followed by CS-BM-FeS_2-CRW11 and CS-WM-FeS_2-CRW11 (Figures S2d−f). These results indicate that CRW11 effectively mitigates corrosion in the welded CS regions with FeS_2 deposits by providing surface coverage, adsorption, and reactivity.

3.1.3. Electrochemical Impedance Spectroscopy. EIS analysis was used to evaluate the CRs of preconditioned test samples.[35] Nyquist plots for CS-BM, CS-WM, and CS-HAZ showed characteristic well-defined semicircular arcs and many with diffusion features at the low-frequency region (Figures S3a−c), which became larger on the addition of the CRW11 inhibitor (Figures S3d−f). Voigt-type EEC models (Figures S3g,h) were used to interpret the data and determine polarization resistance (R_p), which is inversely related to CR, with related corrosion mechanism.[36] The R_p values increased in the order CS-HAZ (173−413 Ω·cm^2) < CS-WM (520−808 Ω·cm^2) < CS-BM (720−880 Ω·cm^2), indicating a corresponding decreasing CR: CS-HAZ (0.74−1.75 mmpy) > CS-WM (0.38−0.58 mmpy) > CS-BM (0.34−0.42 mmpy). The addition of CRW11 significantly increased the diameter of the semicircles of the Nyquist plots, implying effective suppression of CR to below 0.1 mmpy in most cases, with minor exceptions for CS-HAZ and CS-WM at 0 h, which were within the experimental error margin.[37] These results reveal that the inhibitor treatment significantly decreased CRs, except for CS-WM-CRW11 (0.12 mmpy) at 6 h and CS-HAZ-

https://doi.org/10.1021/acs.langmuir.5c02733
Langmuir 2025, 41, 23632−23651

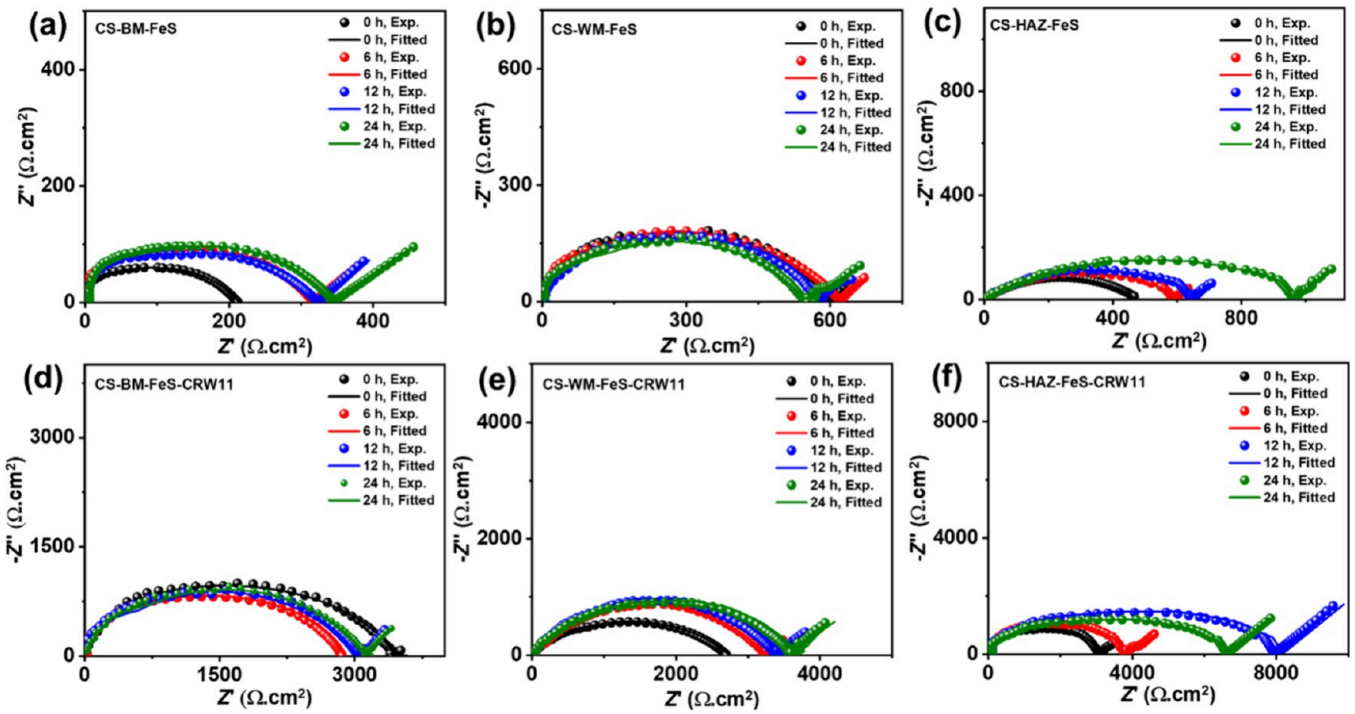

Figure 6. Nyquist plots with preconditioning before corrosion in simulated sour conditions of (a) CS-BM-FeS, (b) CS-WM-FeS, (c) CS-HAZ-FeS, (d) CS-BM-FeS-CRW11, (e) CS-WM-FeS-CRW11, and (f) CS-HAZ-FeS-CRW11.

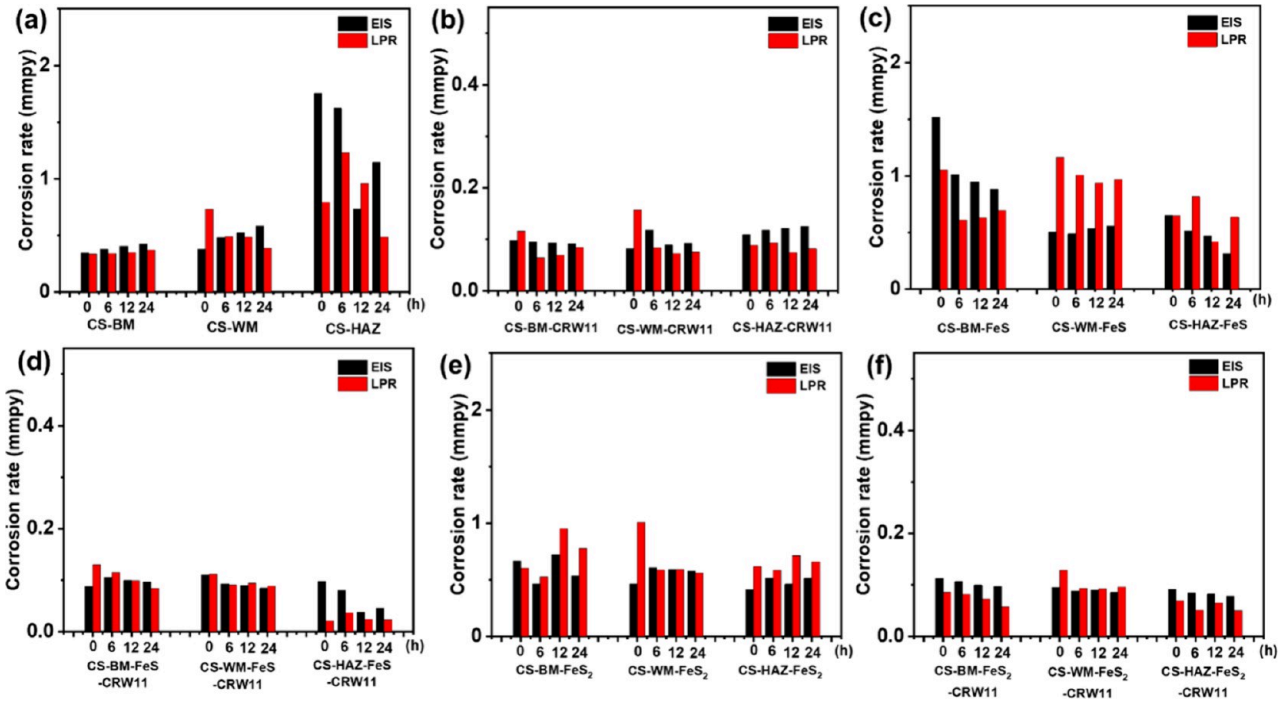

Figure 7. Nyquist plots with preconditioning before corrosion in simulated sour conditions of (a) welded CS, (b) welded CS + CRW11, (c) welded CS + FeS, (d) welded CS + FeS + CRW11, (e) welded CS + FeS_2, and (f) welded CS + FeS_2 + CRW11.

CRW11 (0.11−0.12 mmpy) at all immersion times that were slightly above the threshold. These results show that the CRW11 inhibitor greatly reduced corrosion by significantly suppressing the CRs of the welded CS without deposits in sour conditions.

With FeS-deposited samples, Nyquist plots for CS-BM-FeS, CS-WM-FeS, and CS-HAZ-FeS specimens showed characteristic semicircular arcs with diffusion regions (Figures 6a−c), which expanded upon addition of the CRW11 corrosion inhibitor (Figures 6d−f), using Voigt-type EEC (Figures S3g,h) to extract R_p,[38] as given in the order CS-HAZ-FeS > CS-WM-FeS > CS-BM-FeS. Consequently, CR followed the inverse trend: CS-HAZ-FeS < CS-WM-FeS < CS-BM-FeS. Large semicircles are observed on the addition of the CRW11 inhibitor, which effectively reduced CR to below 0.1 mmpy in most cases, with few exceptions for CS-HAZ-FeS-CRW11 and

https://doi.org/10.1021/acs.langmuir.5c02733
Langmuir 2025, 41, 23632−23651

CS-WM-FeS-CRW11 at 0 h, which fell within the experimental error margin.[39]

EIS was employed to assess the corrosion rates (CRs) of CS specimens with FeS_2 deposits, considering different welding zones and preconditioning method. Nyquist plots revealed characteristic semicircular arcs for all samples (Figures S4a−c), which expanded upon addition of the CRW11 inhibitor (Figures S4e,f). Data fitting using Voigt-type EEC models (Figure S3g,h) yielded R_p values, which decreased in the order CS-HAZ-FeS_2 > CS-WM-FeS_2 > CS-BM-FeS_2. Correspondingly, CR values increased in the reverse sequence with the trend of CS-BM-FeS_2 > CS-WM-FeS_2 > CS-HAZ-FeS_2. The introduction of CRW11 significantly increased the semicircles and reduced CRs for all welded CS samples with FeS_2 deposits to below 0.1 mmpy, demonstrating its effectiveness as a corrosion inhibitor.

3.1.4. Comparative Electrochemical Corrosion Rates. A comparative analysis of CRs from EIS and LPR techniques reveals key insights into the corrosion behavior of welded CS samples under sour service conditions. The CS-HAZ consistently showed the highest CR values, indicating its vulnerability to corrosion in welded CS structures (Figure 7a). The CRW11 inhibitor significantly mitigated corrosion across all regions, achieving IE values over 80% (Figure 7b). The inhibitor's effectiveness varied by region, with CS-HAZ-CRW11 reaching a peak IE (92.4%) immediately upon exposure, while CS-WM-CRW11 (84.9%) and CS-BM-CRW11 (80.4%) achieved maximum IE values at 12 h. This suggests rapid adsorption of CRW11 onto the CS-HAZ surface, providing immediate protection in the sour electrolyte. Comprehensive corrosion data for all regions, obtained from EIS and LPR measurements under simulated sour conditions with and without CRW11, are presented in Table S1.

The corrosion behavior in welded CS with FeS deposit under various conditions, from LPR tests, revealed that CS-WM-FeS was most susceptible to corrosion in FeS-rich environments, followed by CS-BM-FeS and CS-HAZ-FeS. (Figure 7c). The CRW11 inhibitor proved highly effective, achieving IE above 85% for all regions throughout the exposure period. Peak IE varied temporally across regions, with CS-HAZ-FeS-CRW11 reaching 96.4% at 12 h, CS-WM-FeS-CRW11 (91.3% at 24 h), and CS-BM-FeS-CRW11 (87.9% at 24 h) (Figure 7d). This suggests gradual inhibitor penetration of CRW11 through the FeS layer and adsorption onto the CS surface. Comprehensive corrosion data from both EIS and LPR techniques obtained for all welded CS regions with FeS deposits, tested under simulated sour conditions without/with the inhibitor, were compiled in Table S2.

The integrated analysis of EIS and LPR measurements revealed key insights into the corrosion kinetics of preconditioned welded CS specimens exposed to FeS_2 deposits, without/with the CRW11 inhibitor. The CS-BM-FeS_2 consistently showed the highest CRs compared to the CS-WM-FeS_2 and CS-HAZ-FeS_2 in FeS_2-rich environments (Figure 7e). The CRW11 inhibitor demonstrated high IE (>90%) across all metallurgical zones throughout the exposure period. However, peak performance varied temporally, with CS-BM-FeS_2-CRW11 reaching maximum IE at 24 h, while CS-HAZ-FeS_2-CRW11 and CS-WM-FeS_2-CRW11 peaked at 24 and 0 h, respectively (Figure 7f). This suggests a time-dependent penetration mechanism of CRW11 through the FeS_2 layer, with enhanced adsorption stability in the base metal compared to welded regions. Comprehensive quantitative corrosion data for all conditions is summarized in Table S3. Hence, the mechanism of corrosion inhibition of welded CS without/with conductive deposits by CRW1 follows interrelated processes, including surface adsorption (both physisorption and chemisorption) and film formation (reduces water and ion permeation).

3.1.5. Weight Loss Corrosion Studies of Only Base Metal of Carbon Steel. Weight loss corrosion analysis was conducted on base metal samples (CS-BM) without/with the CRW11 inhibitor (CS-BM-CRW11) under simulated sour conditions. Multiple samples were tested at various time intervals to ensure reliability, as summarized in Table S4. At 144 h, the CR for uninhibited samples was 0.50 ± 0.03 mmpy, which decreased significantly to 0.04 ± 0.02 mmpy with the inhibitor (Figure 8). After 336 h, the CR for uninhibited samples reduced to

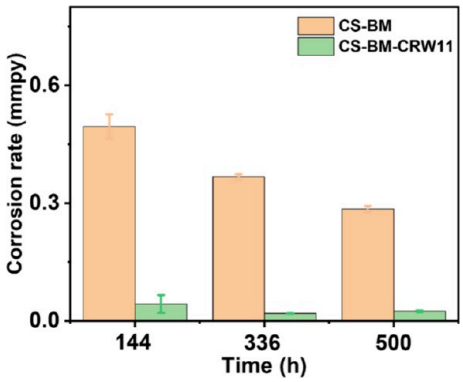

Figure 8. Weight loss corrosion rates for only CS-BM with preconditioning before corrosion tests in absence/presence of CRW11 inhibitor (200 ppm) in simulated sour conditions.

0.37 ± 0.01 mmpy, while inhibited samples showed a CR of 0.02 ± 0.00 mmpy. Similar trends were observed after 500 h. The 336 h weight loss results aligned well with LPR and EIS tests, validating the consistency across methods. However, inhibited samples showed lower CR values in weight loss experiments compared to electrochemical techniques, possibly due to inhomogeneous polarization effects.

3.1.6. Raman Spectra of the Welded Carbon Steel after Corrosion Tests. Raman spectroscopy analysis of the distinct areas of welded CS surfaces (CS-BM, CS-HAZ, CS-WM) exposed to sour conditions revealed distinct corrosion product compositions in uninhibited samples. The corroded CS-BM and CS-HAZ primarily contained hematite (α-Fe_2O_3, 410.0 cm^{-1}),[40] lepidocrocite (γ-FeOOH, 527.6 cm^{-1}),[41] magnetite (Fe_3O_4, 635.3 cm^{-1}),[42] and maghemite (γ-Fe_2O_3, 687.0 cm^{-1}).[41] Conversely, corroded CS-WM showed hematite (α-Fe_2O_3, 290.9 cm^{-1}),[40] Goethite (α-FeOOH, 328.0 cm^{-1}),[41,43] and magnetite, maghemite, and lepidocrocite (Figure 9a). These phases likely originated from aggressive sour electrolyte exposure, with compositional heterogeneity in the weld metal region promoting additional corrosion products.

The introduction of the CRW11 inhibitor led to significant changes in the Raman spectra of inhibited samples across different regions of welded CS samples. CS-BM-CRW11, CS-WM-CRW11, and CS-HAZ-CRW11 each exhibited unique sets of low-intensity peaks, indicating region-specific interactions between the inhibitor and the CS surfaces (Figure 9b). These spectra variations are attributed to differences in local microstructure and elemental composition among the CS-BM,

https://doi.org/10.1021/acs.langmuir.5c02733
Langmuir 2025, 41, 23632−23651

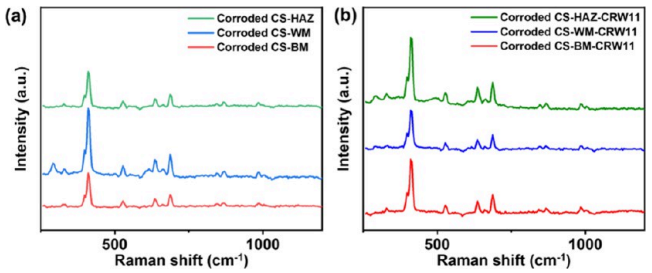

Figure 9. Raman spectra of corroded CS-BM, CS-WM and CS-HAZ after corrosion tests in simulated sour conditions (a) no inhibitor and (b) with CRW11 inhibitor.

CS-HAZ, and CS-WM regions. The distinct corrosion products and their varying complexity in these three regions contribute to the observed differences in corrosion behavior, as reported previously.[44] A comprehensive summary of Raman shifts for all conditions is provided in Table S5.

3.2. Morphology and Elemental Compositions. The elemental compositions of the CS-BM, CS-WM, and CS-HAZ were analyzed using EDX for surface analysis and XRF for bulk analysis. The CS-BM primarily consisted of Fe (91.9 wt %) with minor alloying elements (Table 1). The CS-WM showed slightly lower Fe (89.9 wt %) and Cr (0.2 wt %) contents but higher C and Mn levels, along with the addition of Ni (1.00 wt %) and Zn (1.4 wt %). The CS-HAZ exhibited an intermediate composition. The inclusion of Ni and Zn in the CS-WM was intended to enhance corrosion resistance in sour oil and gas environments, but its effectiveness depends on optimal concentration levels.[45]

XRF analysis revealed the bulk elemental compositions of different regions in welded CS samples. Pristine BM and HAZ showed nearly identical compositions, predominantly consist-

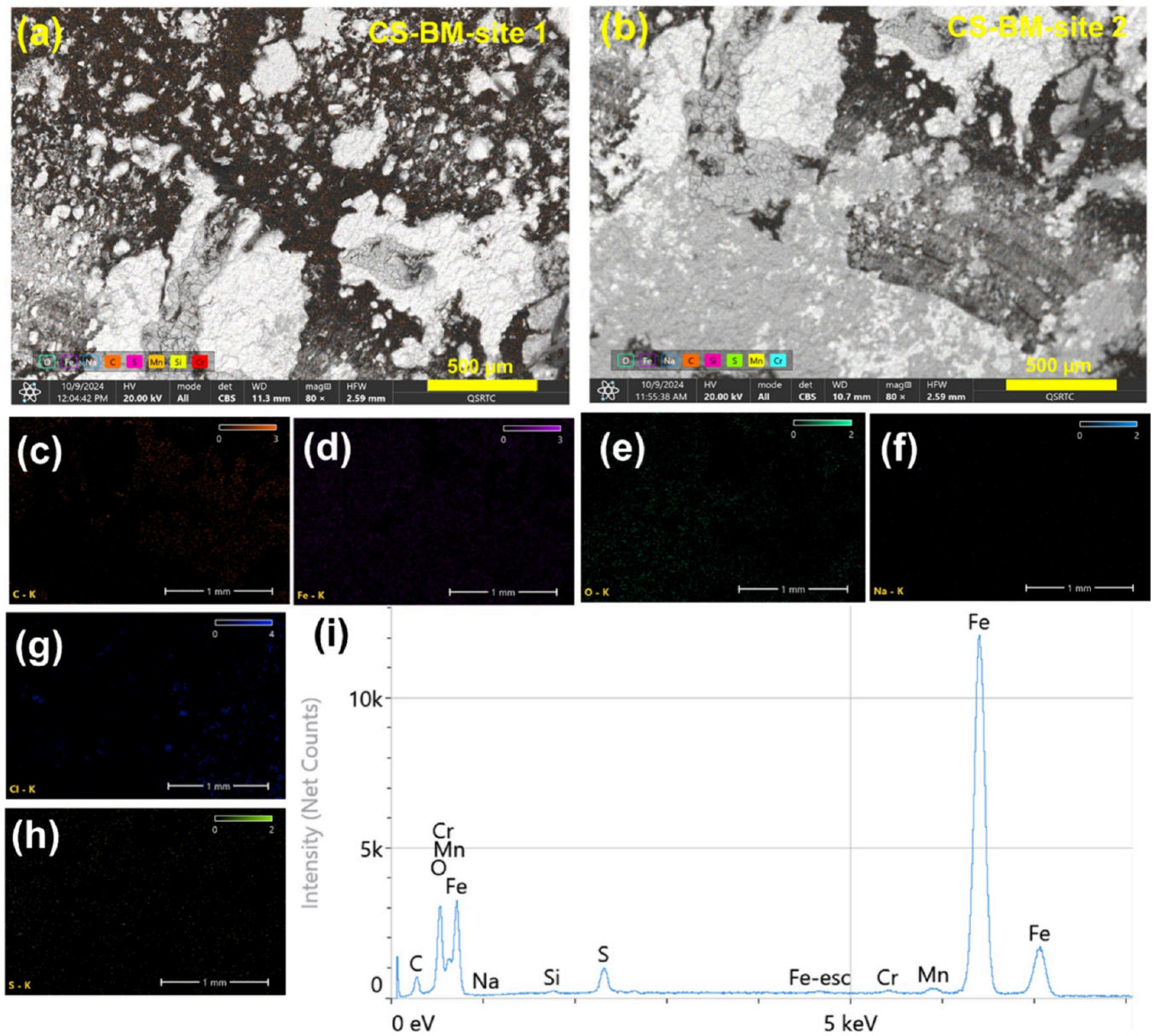

Figure 10. (a, b) SEM micrographs, elemental mapping of (c) C, (d) Fe, (e) O, (f) Na, (g) Cl, and (h) S, and (i) EDX spectra of CS-BM in simulated sour conditions after corrosion tests.

https://doi.org/10.1021/acs.langmuir.5c02733
Langmuir 2025, 41, 23632−23651

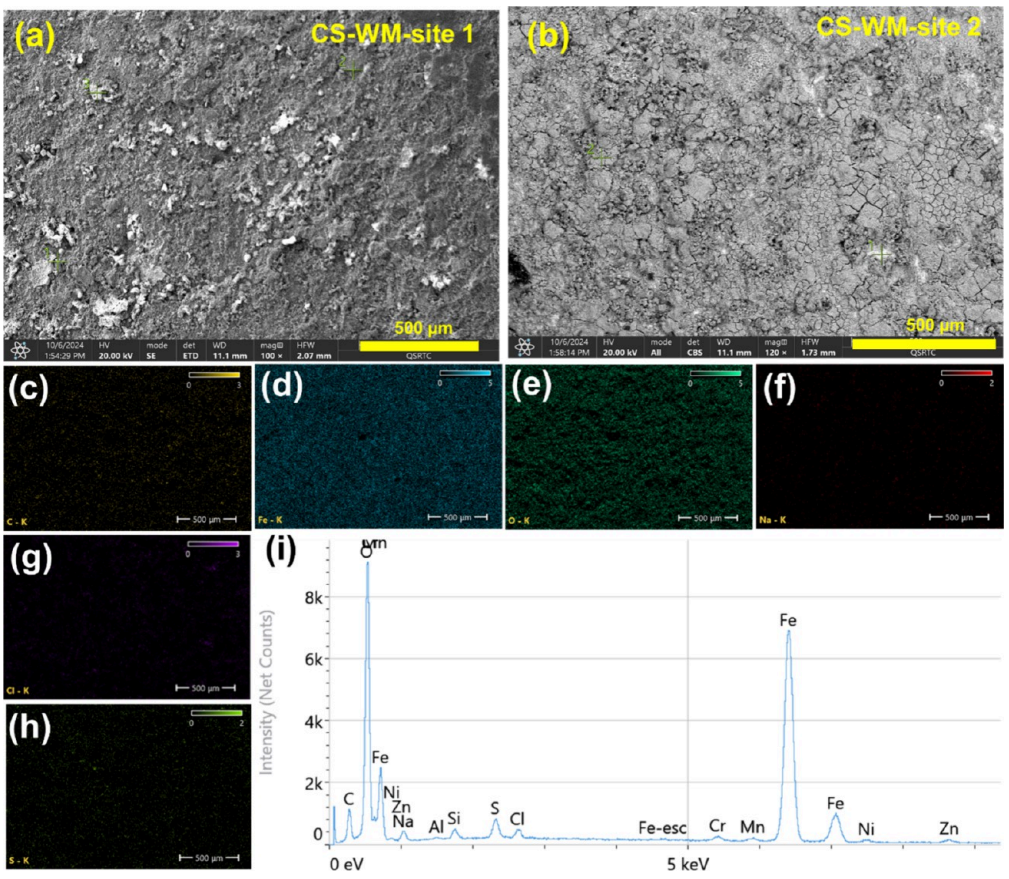

Figure 11. (a, b) SEM micrographs, elemental mapping of (c) C, (d) Fe, (e) O, (f) Na, (g) Cl, and (h) S, and (i) EDX spectra of CS-WM in simulated sour conditions after corrosion tests.

ing of Fe (~97.8 wt %) with trace amounts of Al, Si, Ca, Cr, Mn, Nb, and Mo (Table 1). In contrast, pristine WM exhibited a distinct compositional profile, with Fe (~97.6 wt %) and varying amounts of Al, Si, Cr, Mn, and Mo, as well as unique elements like Sc, Ni, and P. Notably, Ca and Nb were present in BM and HAZ but absent in WM, while Sc, Ni, and P were exclusive to WM. These compositional differences provide insight into the potential variations in behavior during corrosion testing across the welded sample regions. Notably, for the best bulk compositional evaluation, XRF analysis needs a wide exposed area; however, the corroded CS coupons did not have enough surface area for this method. Thus, following corrosion testing, EDX was used to determine the surface elemental compositions of the welded CS coupons.

After corrosion tests, SEM analysis revealed significant surface degradation and corrosion product formation on the CS-BM, CS-WM, and CS-HAZ regions of welded CS samples.[46,47] The original ferritic-pearlite microstructures were largely obscured by corrosion products. The SEM images of CS-BM showed a uniform attack (i.e., no localized corrosive forces), a roughened texture with a matte, granular appearance, no substantial fracture iron sulfide-rich corrosion result, and little protective scale (Figures 10a,b). The SEM images demonstrated that CS-WM and CS-HAZ have loosely adherent rough surfaces with porous and thick iron sulfide layers in addition to localized corrosion with shallow pits and globular product (Figures 11a,b and 12a,b). EDX mapping showed Fe as the predominant element, with varying distributions of O, S, C, and Cl elements across the samples (Figures 10c–h, 11c–h, and 12c–h). Quantitative and qualitative analysis indicated a reduction in Fe content and the presence of corrosion-related elements (Cl, S, O) on all surfaces (Figures 10i, 11i, 12i, and Table S6), suggesting accelerated corrosion in the sour electrolyte environment.[46] CS-WM exhibited the highest adherence to corrosion products, evidenced by increased C, O, and Cl concentrations, followed by CS-HAZ and CS-BM. However, the least Fe content (56.6 wt %) of CS-HAZ proves its highest vulnerability to corrosion in the sour conditions, relative to CS-WM (62.3 wt %) and CS-BM (83.5 wt %). This observation corroborates the findings from the corrosion studies from EIS and LPR.

The addition of the CRW11 inhibitor resulted in mild surface degradation and corrosion product formation across all regions, as proved by SEM micrographs (Figures S5a,b, S6a,b, and S7a,b). EDX mapping showed Fe as the predominant element, uniformly interposed with other elements (Figures S5c–l, S6c–l, and S7c–l). The inhibitor appeared to interact with the CS samples, reducing the formation of corrosion products in the sour electrolyte environment. This result was evidenced by increased C and Fe contents, particularly in the CS-HAZ-CRW11, and elevated Na levels (Figures S5m, S6m, S7m, and Table S6). The CRW11 inhibitor effectively mitigated corrosion rates and reduced the formation of corrosion products (Cl, S, and O). This observation is consistent with previous reports.[31,48]

SEM analysis revealed significant corrosion and surface degradation on welded CS samples with FeS deposits (Figures S8a,b, S9a,b, and S10a,b). EDX mapping showed elemental distribution, with Fe being the primary element, along with

https://doi.org/10.1021/acs.langmuir.5c02733
Langmuir 2025, 41, 23632−23651

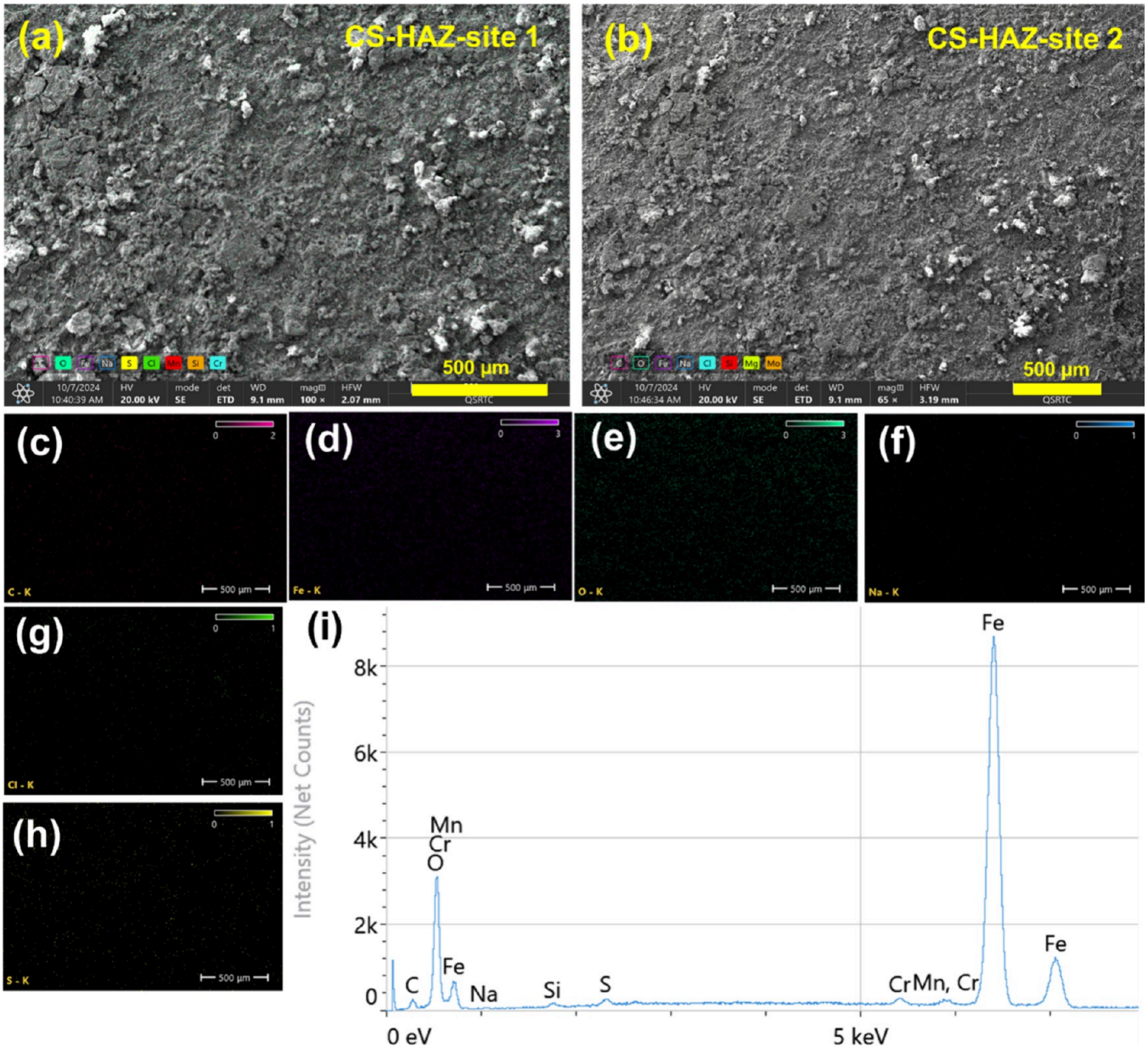

Figure 12. (a, b) SEM micrographs, elemental mapping of (c) C, (d) Fe, (e) O, (f) Na, (g) Cl, and (h) S, and (i) EDX spectra of CS-HAZ in simulated sour conditions after corrosion tests.

traces of Mn, Si, Al, Ca, and Cr (Figures S8c–k, S9c–k, and S10c–l). O- and S-based corrosion products were prevalent across all specimens. Notably, pitting was observed in the CS-WM-FeS and CS-HAZ-FeS. C and C showed varied distribution patterns, with Cl uniformly spread on CS-BM-FeS and CS-WM-FeS samples but concentrated on one side of the CS-HAZ-FeS. The qualitative and quantitative EDX analysis revealed elevated Fe content in samples with deposits compared to those without, indicating FeS deposition. All surfaces showed significant presence of Cl, S, and O, suggesting accelerated corrosion in the sour electrolyte environment (Figures S8l, S9l, S10m, and Table S7). CS-HAZ-FeS has predominantly increased C, S, and Cl distribution and concentration, which may be traced to the predominant reactions at the HAZ regions with FeS deposit. Meanwhile, the main corrosion products present in CS-WM-FeS were C, S, O, and Cl, while CS-BM-FeS has high amounts of O and Na. Thus, the FeS deposit allows a larger amount of O and Na presence in CS-BM-FeS, making it more susceptible to rapid corrosion compared to CS-WM-FeS and CS-HAZ-FeS.

The addition of the CRW11 inhibitor results in moderate surface degradation and corrosion product formation across all three regions of the welded CS samples with FeS deposits.[49] SEM images reveal these effects (Figures S11a,b, S12a,b, and S13a,b), while EDX mapping shows the spatial distribution of elements on the surfaces (Figures S11c–j, S12c–l, and S13c–k). Fe is identified as the predominant element, uniformly interspersed with Mn, Si, Mo, Cr, and Ca. The results reveal that CRW11 effectively reduces the formation of O- and S-based corrosion products. Elemental mapping and quantitative EDX analysis show distinct compositions for CS-BM-FeS-CRW11, CS-WM-FeS-CRW11, and CS-HAZ-FeS-CRW11 samples (Figures S11k, S12m, S13l, and Table S6). Notably, Cl was absent in CS-BM-FeS-CRW11 and CS-HAZ-FeS-

https://doi.org/10.1021/acs.langmuir.5c02733
Langmuir 2025, 41, 23632−23651

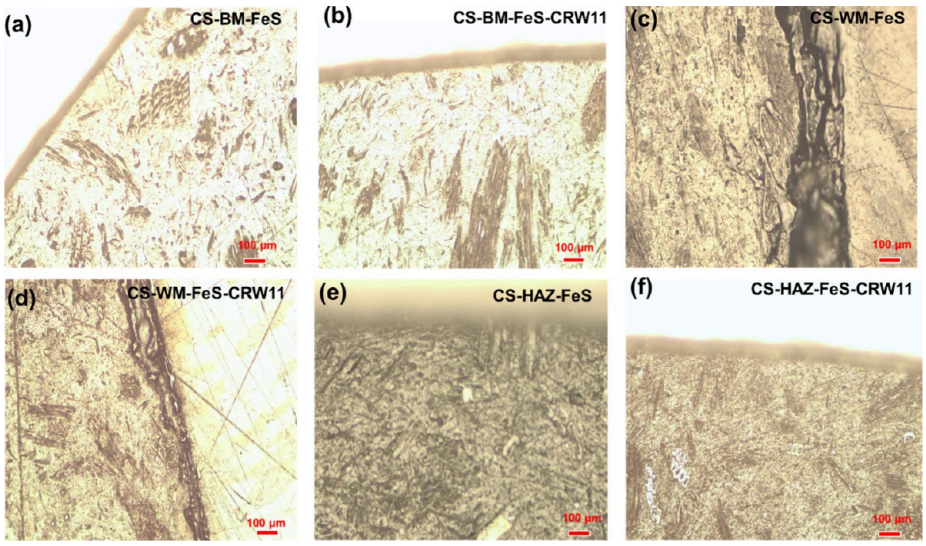

Figure 13. OM images of (a) CS-BM-FeS, (b) CS-BM-FeS-CRW11, (c) CS-WM-FeS, (d) CS-WM-FeS-CRW11, (e) CS-HAZ-FeS, (f) CS-HAZ-FeS-CRW11.

CRW11 samples but present in CS-WM-FeS-CRW11. The elevated levels of C, O, and Fe, particularly in the CS-WM-FeS-CRW11, indicate a strong interaction between the welded CS samples and the CRW11 inhibitor. This interaction appears to reduce the formation of corrosion products in a sour electrolyte environment, mitigating overall corrosion rates through inhibitory action on corrosion product formation mechanisms.

SEM analysis of welded CS samples with FeS_2 deposits revealed severe surface degradation and corrosion product accumulation across CS-BM-FeS_2, CS-WM-FeS_2, and CS-HAZ-FeS_2 regions (Figures S14a,b, S15a,b, and S16a,b). EDX mapping identified Fe as the dominant element (56.00−68.20 wt %), uniformly distributed with Mn, Si, and Cr (Figures S14c−k, S15c−k, and S16c−k), while concentrated O/S species clusters and variable Cl,C, and O distributions indicated localized corrosion mechanisms.[50] CS-WM-FeS_2 exhibited elevated O (25.57−39.27 wt %) and S (0.60−1.07 wt %) concentrations (Figures S14l, S15l, S16l, and Table S8), accompanied by S and O dominated corrosion products, whereas CS-HAZ-FeS_2 showed pronounced Cl accumulation.[51] These patterns, coupled with increased Fe content and S−O−Cl synergy compared to nondeposited samples, demonstrate accelerated corrosion in sour environments, with CS-WM-FeS_2 and CS-HAZ-FeS_2 exhibiting more adherence of corrosion products due to microstructural heterogeneities.[52]

The incorporation of the CRW11 corrosion inhibitor caused moderate surface deterioration and uniform deposition of corrosion products on FeS_2-laden welded CS substrates across the CS-BM-FeS_2-CRW11, CS-WM-FeS_2-CRW11, and CS-HAZ-FeS_2-CRW11, as shown by SEM analysis (Figures S17a,b, S18a, and S19a,b). EDX spectroscopy confirmed Fe as the primary element (71.93−77.63 wt %) with dispersed Mn, Si, and Cr, while O, S, and Cl distributions indicated reduced inhibitor effectiveness due to FeS_2 deposits (Figures S17c−l, S18b−k, and S19c−l). However, CRW11 limited subsurface propagation of corrosive species. Quantitative analysis revealed distinct elemental variations: CS-BM-FeS_2-CRW11 had higher S (3.13 wt %) and C (3.14 wt %); CS-WM-FeS_2-CRW11 showed elevated Na (1.24 wt %) and Cl (0.43 wt %); and CS-HAZ-FeS_2-CRW11 retained the highest Fe content (77.63 wt %) with minimal S (0.26 wt %) and Cl (0.02 wt %) (Figures S17m, S18l, S19m, and Table S8). Elevated concentrations of Fe and O in CS-HAZ-FeS_2-CRW11 samples indicate strong interfacial interactions between CRW11 and the CS matrix, which correspond to reduced Cl (0.02−0.43 wt %) and S (0.26−3.13 wt %) accumulation compared to uninhibited controls. This implies that CRW11 influences corrosive anion adsorption kinetics in sour media, stabilizing the iron oxide layer and mitigating corrosion by suppressing FeS_2-mediated oxidation pathways.

3.3. Microstructures of Welded Carbon Steel. The microstructural evaluation of welded CS coupons revealed distinct phase distributions across the pristine BM, pristine WM, and pristine HAZ. Optical microscopy (OM) showed the BM with a ferrite-pearlite matrix and elongated grain boundaries, marked in red color (Figure S20a), indicative of partial recrystallization during thermo-mechanical processing. Also, various construction angles (0−90°) and the waveform interface posed significant effects on the microstructure and mechanical properties of X65 welded CS.[53] The WM exhibited a δ-ferrite-dominated microstructure with cellular/columnar dendritic structures, besides martensite-austenite (M-A) constituents and intragranular acicular ferrite, with interconnected grain boundaries (marked in red color) and no pearlite or microcracks (Figure S20b). In contrast, the HAZ displayed bainitic transformation products, sparse M-A phases, and fine-grained ferritic regions, without pearlite or stress-induced cracking (Figure S20c). These variations arise from localized thermal gradients and diffusional kinetics during welding, promoting metastable microconstituents over equilibrium phases.[54] The WM's martensitic phase is particularly vulnerable to corrosion under sour conditions because of its high hardness, high internal stresses, and high density of lattice cracks.[55] Likewise, the presence of granular bainite in the HAZ results in decreased corrosion resistance due to its coarse microstructure with large grain boundaries (marked in red color in Figure S20c) and inadequate passivation properties.[56,57] These features could be caused by the welding heat input at the HAZ, which could increase its corrosion rates and make it the most vulnerable area. In contrast to the WM and

https://doi.org/10.1021/acs.langmuir.5c02733
Langmuir 2025, 41, 23632−23651

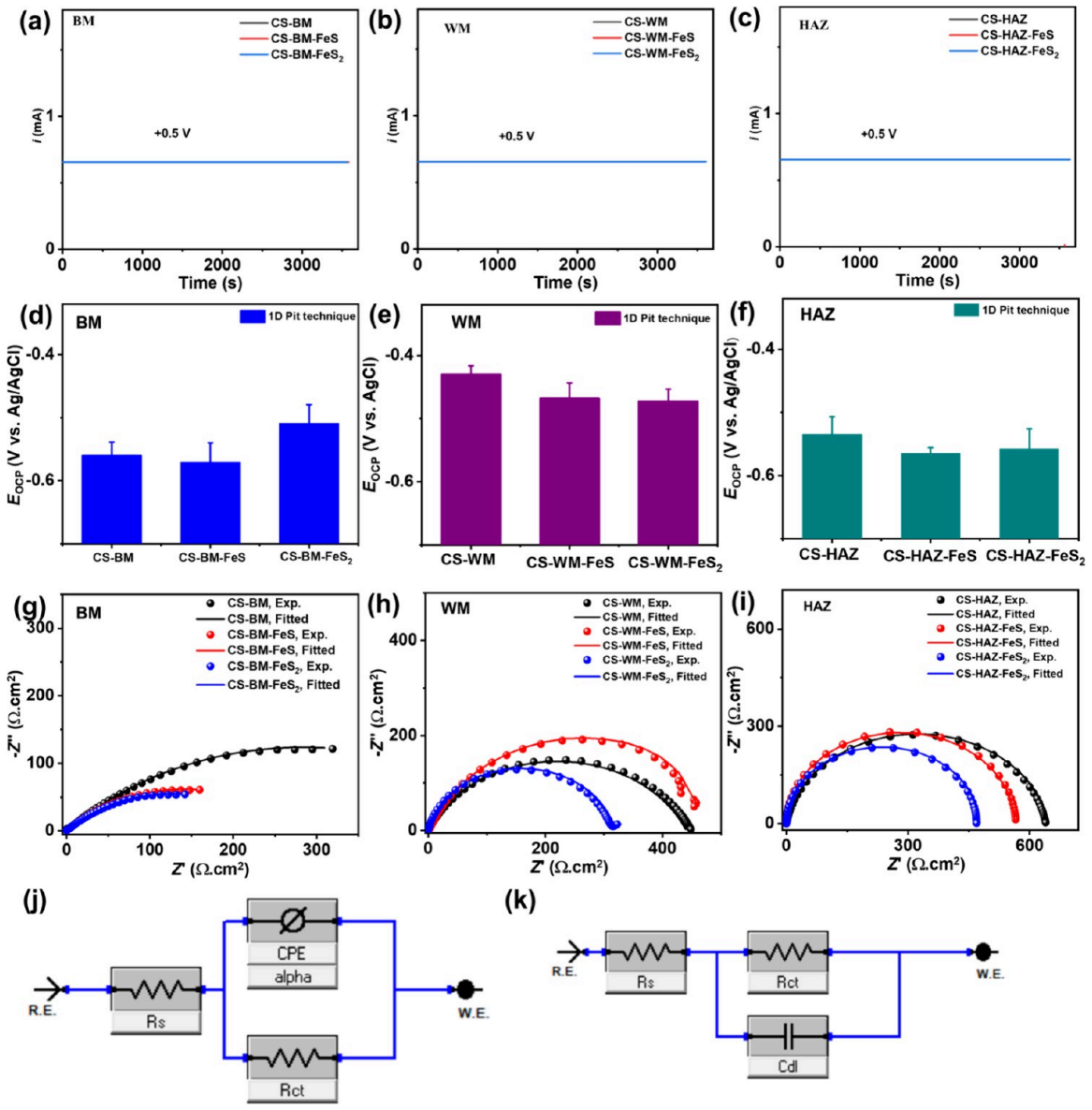

Figure 14. (a–c) Potentiostatic at +500 mV, (d–f) OCP for 100 s, (g–i) Nyquist plots, and (j, k) Voigt EEC models of welded CS wires (1 mm) without/with deposits (FeS and FeS_2) for 1D-artificial pit growth and propagation in simulated sour conditions.

HAZ, the BM with a ferrite-pearlite matrix exhibits better corrosion resistance because of its more refined microstructure and improved capacity to build passive protective layers.[56]

The microstructural analysis of corroded welded CS samples revealed significant corrosion-induced changes, without deposits and with the absence/presence of the CRW11 inhibitor. OM showed grain boundary attack and corrosion product formation, including O, S, C, and Cl. In the corroded CS-BM (Figure S20d), grain boundary attack was masked by corrosion product deposition,[58] while the corroded CS-WM (Figure S20f) and corroded CS-HAZ (Figure S21h) experienced severe grain boundary attack, leading to structural deformation. This is indicative of preferential weldment corrosion due to the severity of the corrosive assault on the microstructural integrity and composition of these regions.[59] The CS-HAZ was particularly vulnerable due to its fine-grain structure with a high grain boundary area.[48b] However, applying the CRW11 inhibitor significantly reduced grain boundary attack and corrosion product deposition by forming a protective hydrophobic barrier and scavenging oxygen.[34,60] This preserved the original microstructural features across all regions (CS-BM-CRW11, CS-WM-CRW11, and CS-HAZ-CRW11, Figures S20e,g,i). The results demonstrate the inhibitor's effectiveness in maintaining microstructural integrity under corrosive conditions.

The deposition of FeS on welded CS coupons, i.e., CS-BM-FeS, CS-WM-FeS, and CS-HAZ-FeS, induces microstructural changes that drive corrosion variability. In CS-BM-FeS (Figure 13a), there was grain boundary disruption that promotes boundary failure,[61] while in CS-WM-FeS and CS-HAZ-FeS (Figure 13c,e), there are precipitates of FeS along grain boundaries increasing ferrite contact area and weakening boundary cohesion.[62] Localized pitting arises from electrochemical potential differences between unstrained ferrite and grain boundary defects,[63] with CS-WM-FeS showing the highest corrosion susceptibility due to intensified galvanic activity. The addition of the CRW11 inhibitor mitigates corrosion by forming a protective interfacial film at FeS-CS

https://doi.org/10.1021/acs.langmuir.5c02733
Langmuir 2025, 41, 23632−23651

boundaries (Figure 13b,d,f), suppressing anodic/cathodic currents and raising activation energy barriers to slow degradation.[64]

The presence of FeS_2 deposit in three distinct regions of welded samples, i.e., CS-BM-FeS_2, CS-WM-FeS_2, and CS-HAZ-FeS_2, causes significant microstructural changes, leading to heterogeneous corrosion rates.[65] In CS-BM-FeS_2 (Figure S21a), FeS_2 deposit alters grain boundary morphology, causing grain boundary failure. In CS-WM-FeS_2 (Figure 21c) and CS-HAZ-FeS_2 (Figure 21e), FeS_2 deposit precipitates accumulate at grain boundaries, increasing interfacial contact with ferrite grains and compromising boundary integrity. This promotes localized corrosion due to electrochemical potential differences between the ferrite matrix and defects or secondary phases, with CS-WM-FeS and CS-WM-FeS_2 showing the highest microstructural deformation due to intergranular oxidation and high-energy grain boundaries. A similar observation had previously been reported.[65,66] The addition of the CRW11 inhibitor to the sour electrolyte forms a protective film at the FeS_2−CS interface (Figures 21b,d,f). This reduces anodic and cathodic current densities, increasing energy activation for corrosion, and slowing overall corrosion kinetics. Hence, the FeS and FeS_2 increase the CRs of the welded CS sample regions in the simulated sour conditions.

3.4. 1D Artificial Pit Technique. The kinetics of pitting corrosion in welded CS wires were studied using the 1D artificial pit technique, enabling controlled analysis of pit growth. Electrodes (1 mm diameter) were fabricated and tested at three welded regions, without/with deposits (FeS and FeS_2), under simulated sour conditions. Potentiostatic at +500 mV *vs.* Ag/AgCl for 1 h revealed consistent pit growth across all regions, even with conductive deposits (Figures 14a−c). Identical experimental conditions highlighted no significant differences in pit initiation and growth among the regions, suggesting uniform susceptibility to pitting corrosion.

The pitting corrosion behavior of 1D welded CS wires without/with deposits (FeS and FeS_2) was examined using OCP and EIS. OCP results showed slight variations in the pitting corrosion potential of the CS-BM, with FeS_2 making it most anodic, then FeS (Figure 14d). For the CS-WM (Figure 14e), more positive anodic OCP values were observed, indicating it as the most anodic region without/with the conductive deposits in sour conditions. CS-HAZ (Figure 14f) exhibited anodic behavior similar to the CS-BM, with FeS_2 inducing the highest anodicity on CS-BM. Overall, the CS-WM displayed more oxidation tendencies (i.e., anodic), while the CS-BM and CS-HAZ were cathodic (Figure S22a). However, the potential differences across regions were below 150 mV, insufficient to cause severe galvanic coupling in sour electrolytes.

Pitting resistance (R_{pit}) was determined using EIS, with Nyquist plots displaying deformed or well-defined semicircular arcs for CS-BM, CS-WM, and CS-HAZ in sour electrolyte, both without/with FeS and FeS_2 deposits (Figures 14g−i). EIS parameters were analyzed using Voigt EEC models (Figures 14j,k). For the CS-BM, R_{pit} decreased in the order CS-BM > CS-BM-FeS > CS-BM-FeS_2, correlating to increasing pit current densities (i_{pit}, CS-BM < CS-BM-FeS < CS-BM-FeS_2) and pit propagation rates. FeS_2 deposits caused the highest pit propagation rate: CS-BM-FeS_2 (1.19 mmpy), CS-WM-FeS_2 (0.97 mmpy) and CS-HAZ-FeS_2 (0.65 mmpy) (Figure S21b). Using Faraday's second law, pit depths (d_{pit}) were calculated from three different experiments, yielding average values of 29.7 ± 0.6 μm, 59.3 ± 1.8 μm, 66.7 ± 2.0 μm for CS-BM, CS-BM-FeS and CS-BM-FeS_2, respectively (Figure S22c). In the CS-WM, the R_{pit} was in the trend of CS-WM > CS-WM-FeS > CS-WM-FeS_2, with CS-WM-FeS_2 showing the highest pit propagation rate and d_{pit}. In the CS-HAZ, the R_{pit} sequence differed: CS-HAZ > CS-HAZ-FeS > CS-HAZ-FeS_2, where CS-HAZ-FeS_2 exhibited the highest pit propagation rate and d_{pit}. These findings suggest that deposits influence pitting differently in various regions with specific combinations, and FeS_2 produces the deepest pits in their respective welding zones. A detailed summary of electrochemical pit growth, propagation, and calculated pit depth is provided in Table S9.

Pitting corrosion was quantitatively analyzed using optical microscopy (OM) on 1D artificial pits, with results aligning closely with calculated d_{pit}. Initial examination of polished welded CS wires revealed no visible pitting in the BM, WM, and HAZ (Figures S23a−c). Following exposure to simulated sour conditions, OM profiling was used to assess pitting parameters on welded CS wires, without/with FeS and FeS_2 deposits. Micrographs showed distinct pit propagation in CS-BM, CS-WM, and CS-HAZ regions under these conditions. Quantitative analysis of these images provided detailed data on pitting behavior, detailed in Table 2.

Table 2. Parameters obtained from optical microscopes after 1D artificial pit technique of welded CS wires without/with deposits in simulated sour conditions

samples	actual d_m (μm)	aspect ratio	pit area (mm^2)	pit density (mm^{-2})
Base Metal				
CS-BM	34.9 ± 7.9	3.0 ± 0.8	0.008	123.0
CS-BM-FeS	71.4 ± 11.8	1.5 ± 0.2	0.009	114.0
CS-BM-FeS_2	69.0 ± 11.7	1.6 ± 0.3	0.009	112.4
Welding Metal				
CS-WM	40.8 ± 4.2	2.6 ± 0.3	0.009	116.7
CS-WM-FeS	43.6 ± 11.1	2.5 ± 0.7	0.009	117.7
CS-WM-FeS_2	46.0 ± 3.6	2.1 ± 0.1	0.008	133.0
Heat Affected Zone				
CS-HAZ	23.2 ± 0.7	4.5 ± 0.4	0.008	119.8
CS-HAZ-FeS	34.2 ± 2.5	2.3 ± 0.5	0.005	198.4
CS-HAZ-FeS_2	23.1 ± 7.5	2.1 ± 0.4	0.002	568.0

For CS-BM and its deposit variants (Figure S24), d_{pit} varied from 34.9 ± 7.9 to 71.4 ± 11.8 μm, with aspect ratios of 1.5 ± 0.2 to 3.0 ± 0.8, pit areas ranging from 0.008 to 0.009 mm^2, and pit densities between 112.4 and 123.0 mm^{-2} (Figures S22d−f and Table 2). Among these, CS-BM-FeS had the greatest pit depth and density, while CS-BM exhibited the highest aspect ratio and pit density.

For CS-WM and its deposit variants (Figure 15), d_{pit} ranged from 40.8 ± 4.2 to 48.7 ± 7.74 μm, with aspect ratios between 1.9 ± 0.5 and 2.6 ± 0.3, pit areas spanning 0.006 to 0.009 mm^2, and pit densities from 113.2 to 176.6 mm^{-2} (Figures S22d−f and Table 2). Among these, CS-WM-FeS_2 displayed the greatest pit depth and area, CS-WM-FeS_2 had the highest pit density, and CS-WM exhibited the largest aspect ratio and pit area.

For CS-HAZ and its deposit variants (Figure S25), d_{pit} ranged from 23.1 ± 7.5 to 44.5 ± 2.3 μm, with aspect ratios between 2.1 ± 0.4 and 4.5 ± 0.4, pit areas spanning 0.002 to 0.008 mm^2, and pit densities from 119.8 to 568.0 mm^{-2} (Figures S22d−f and Table 2). Among the variants, CS-

https://doi.org/10.1021/acs.langmuir.5c02733
Langmuir 2025, 41, 23632−23651

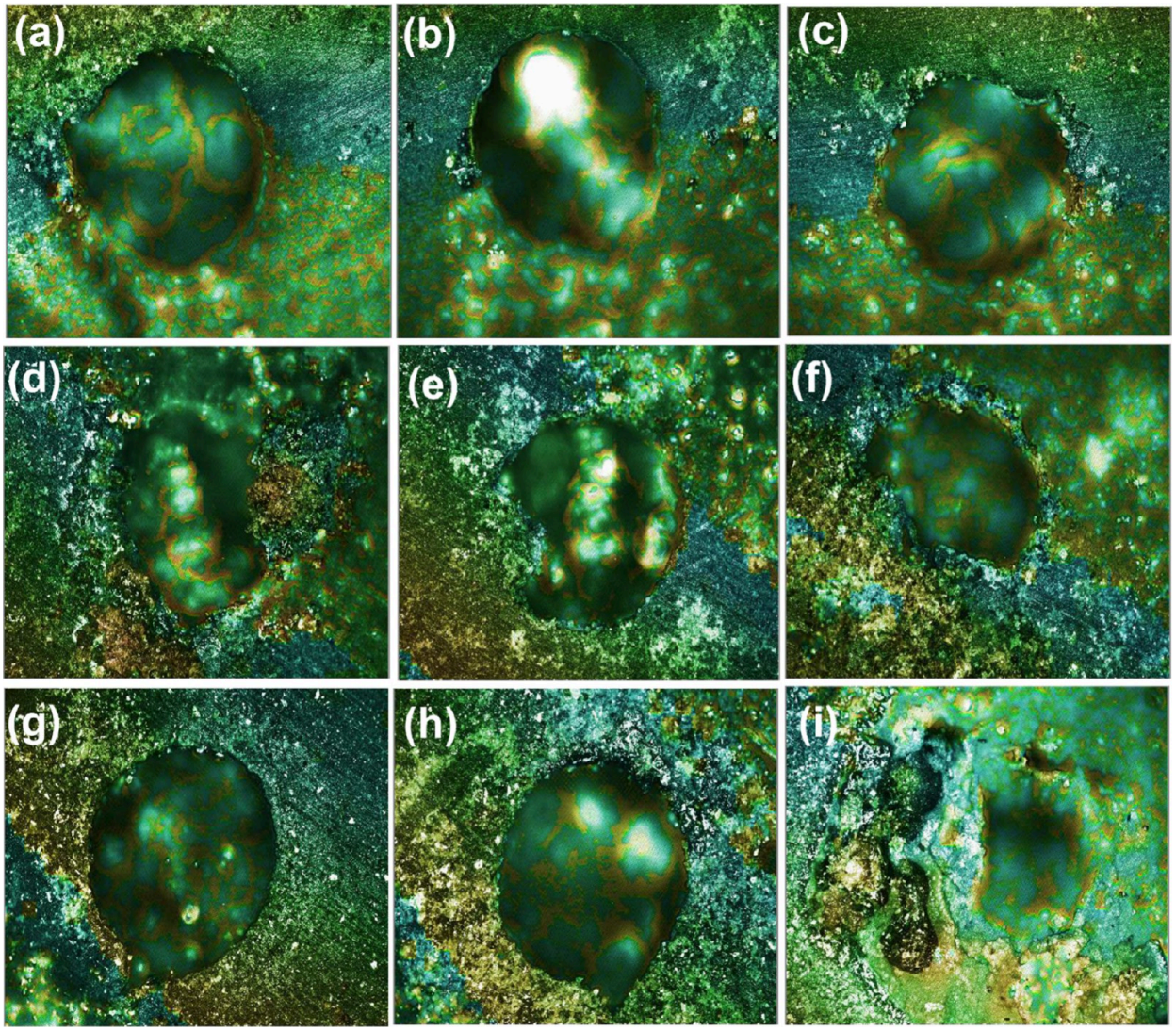

Figure 15. Optical microscope images of (a–c) CS-WM (d–f) CS-WM-FeS, and (g–i) CS-WM-FeS_2 after 1D-artificial pit tests in sour conditions.

HAZ-FeS had the greatest pit depth, CS-HAZ exhibited the highest aspect ratio and pit area, and CS-HAZ-FeS_2 showed the highest pit density, highlighting distinct pitting corrosion behaviors influenced by deposit type and morphology distribution across welded CS regions. Notably, small to irregular pits occur around the sulfide inclusions with FeS and FeS_2 deposits, and as time passes, the pit's area and perimeter grow. In these changing pits, the current density rises in response to the kinetics of pit cover rupture and dissolving brought on by the FeS and FeS_2 deposits. As a result, the FeS and FeS_2 cause dynamic pit growth and chemical effects on the welded CS.

3.5. Applicability of Machine Learning Algorithms. This study utilized ML frameworks to predict localized corrosion behavior in welded CS under simulated sour conditions, incorporating diverse experimental parameters. These include welded regions (CS-BM, CS-WM, and CS-HAZ), conductive deposits (FeS and FeS_2), corrosion inhibitor (CRW11) presence, and sour conditions. A data set of 144 points was compiled from LPR and EIS measurements, addressing limitations of prior studies that relied on single techniques.[20,67] Categorical variables like weld regions, deposit types, and inhibitor status were encoded via one-hot vectors, with IE as the target output. The data was split into training (80%) and testing (20%) subsets, ensuring proportional representation of electrochemical methods. Seven regression algorithms (i.e., LR, SVR, KNN, RF, DT, GB, and XGBoost) were evaluated using R^2, RMSE, and MAE metrics. This approach represents a significant advancement by integrating multimodal data for enhanced corrosion prediction.[68]

The cumulative correlation matrix of welded CS samples across three regions, i.e., CS-BM, CS-WM, and CS-HAZ, was analyzed under sour conditions with and without the CRW11 inhibitor (Figure 16a). ML algorithms were applied to the input data, and their performance was evaluated by comparing actual versus predicted values (Figure 16b). Validation tests demonstrated that RF and DT regressors achieved high R^2 (0.99) values with no RMSE/MAE (Figure 16c), confirming their suitability for predicting the behavior of welded CS samples without deposit under these conditions. A detailed summary of model performance metrics is provided in Table 3.

The correlation matrix of welded CS samples with FeS deposits (CS-BM-FeS, CS-WM-FeS, and CS-HAZ-FeS) was analyzed under sour conditions, with and without the CRW11 inhibitor (Figure 16d), to integrate the input data into ML algorithms. RF and DT regressors demonstrated superior

https://doi.org/10.1021/acs.langmuir.5c02733
Langmuir 2025, 41, 23632–23651

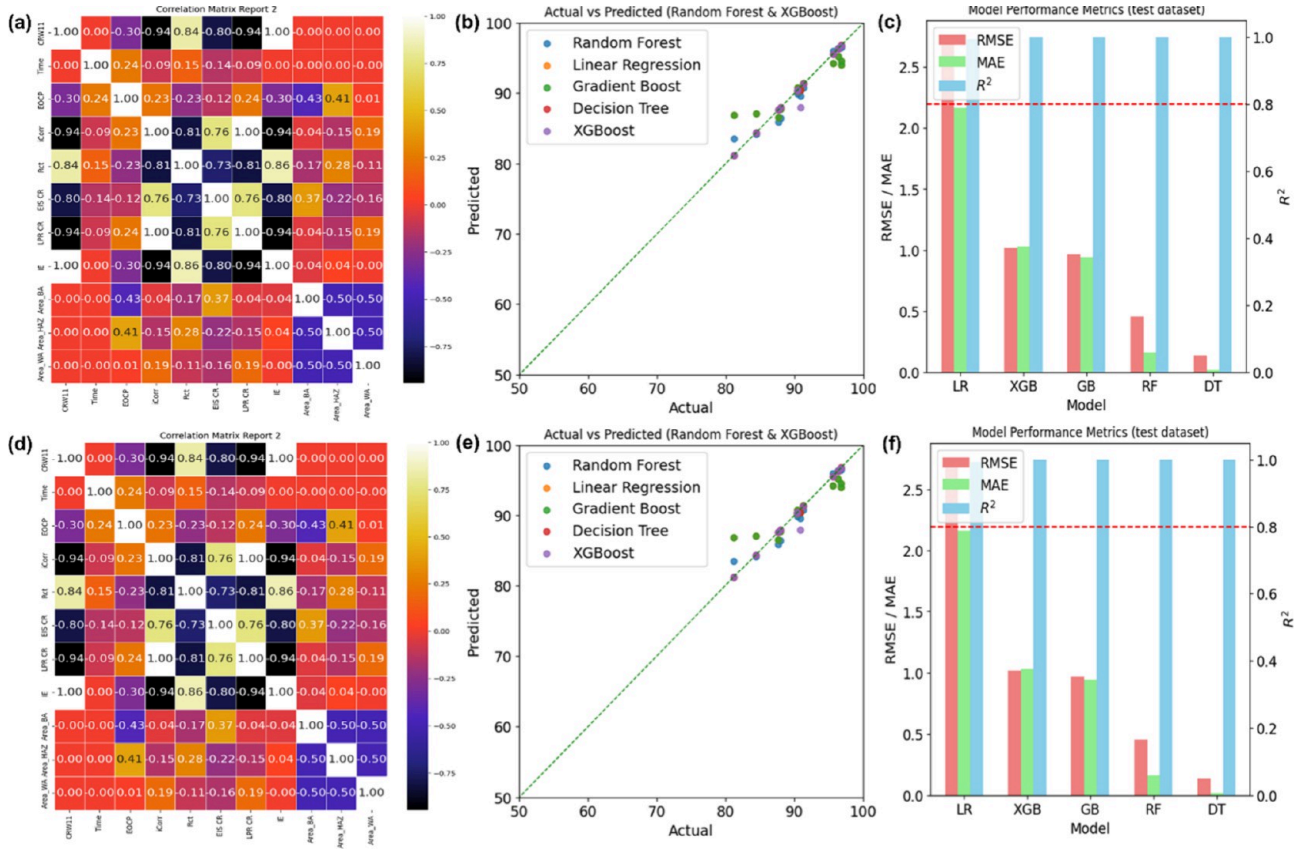

Figure 16. Correlation matrix of entire data set, comparison of actual vs predicted IE using LR DT, RF, GB, and XGB regressors, and models performance metrics for testing data sets of (a−c) welded CS and (d−f) welded CS + FeS deposit in absence/presence of CRW11 inhibitor in sour conditions.

Table 3. Summary of ML Algorithms Performance Metrics for Welded CS Samples, without/with Deposits (FeS or FeS_2) in the Presence of CRW11 Inhibitor in Sour Conditions

	Test data metrics (no deposit)			Test data metrics (with FeS deposit)			Test data metrics (with FeS_2 deposit)		
ML models	R^2	RMSE	MAE	R^2	RMSE	MAE	R^2	RMSE	MAE
LR	0.98	3.3	2.8	0.99	2.8	2.1	0.99	3.8	2.8
RF	0.99	0.2	0.1	0.99	0.2	0.1	0.99	1.0	1.0
GB	0.99	1.0	1.0	0.99	1.0	1.0	0.99	1.3	1.6
DT	0.99	0.7	0.5	0.99	0.1	0.1	0.99	1.0	1.0
XGBoost	0.99	0.8	0.7	0.99	1.0	1.0	0.99	0.1	0.1

predictive performance, achieving high R^2 (0.99) and insignificant RMSE/MAE during validation. Figure 16e highlights the comparison of actual versus predicted values for top-performing models, while Figure 16f confirms their accuracy through testing the behavior of welded CS coupons with FeS deposits under varying conditions (Table 3).

The correlation matrix of welded CS samples with FeS_2 deposits (CS-BM-FeS_2, CS-WM-FeS_2, and CS-HAZ-FeS_2) was analyzed under sour conditions, without/with the CRW11 inhibitor, to integrate data into ML algorithms (Figure S26a−c). The resulting data compared actual and predicted values for top-performing models, revealing that XGBoost and RF models achieved near perfect R^2 (0.99) value and least RMSE/MAE values (Table 3), demonstrating excellent predictive capabilities for the behavior of welded CS coupons with FeS_2 deposit under sour conditions. These findings quantitatively support algorithm selection for predicting corrosion behavior in such samples, with model performance metrics.

Feature importance analysis revealed electrochemical parameters, specifically R_p from EIS and i_{corr} from LPR were the most influential predictors of IE Additionally, categorical variables like deposit type (FeS or FeS_2) and welded CS regions (CS-BM, CS-WM, CS-HAZ) contributed significantly to model outputs, aligning with experimental trends in corrosion susceptibility. These relationships are also visually evident in the correlation plots (Figures 16a,d and S26a), where strong associations between these input features and IE can be observed across different sample conditions. This visual correlation supports the relevance of these features in the predictive modeling framework. Moreover, inhibition power (IP) was evaluated as an additional target variable alongside IE. We found that model performance in predicting IP was similar to that of IE, owing to their high correlation across the data set. This justifies our focus on IE on the main ML results, while

https://doi.org/10.1021/acs.langmuir.5c02733
Langmuir 2025, 41, 23632−23651

still supporting the broader applicability of the models. This comparison reinforces our conclusion that RF and XGBoost models are most suitable for accurately predicting both IE and IP under the sour conditions

4. CONCLUSIONS

This work addresses the interaction of microstructure, elemental compositions, and mitigation measures of X65 welded CS pipes in sour environments to provide a thorough understanding of PWC and pitting corrosion. The key findings are highlighted as follows:

- Corrosion mechanisms and hierarchies, where CRs increased in the sequence of CS-BM (0.34−0.42 mmpy) < CS-WM (0.38−0.73 mmpy) < CS-HAZ (0.48−1.75 mmpy), are among the important findings of the inquiry that are demonstrated by electrochemical analyses (EIS and LPR). Deposition of conductive FeS or FeS_2 deposits increased localized acidity and potential variations between weldment locations, further aggravating this hierarchy.
- The welding sections' (i.e., CS-WM and CS-HAZ) vulnerability to localized attack was highlighted by the notable microstructural and elemental compositional alterations that were seen both before and after corrosion tests, evidenced by SEM, microstructures, and EDX.
- With IE (>80%), the amine-based CRW11 inhibitor showed remarkable efficacy in lowering CRs below the crucial 0.1 mmpy threshold. This was accomplished by scavenging oxygen and forming protective layers, which reduced microgalvanic interactions.
- Raman spectroscopy was used to identify important corrosion products, such as α-Fe_2O_3, γ-FeOOH, and Fe_3O_4. Also, the studies of artificial pits showed the kinetics of pit propagation, especially under FeS-induced heterogeneity, with CS-BM-FeS having the highest pit depth (71.4 ± 11.8 μm), but increased pit density (568.0 mm^2) recorded in CS-HAZ-FeS_2. This implies the impact of various conductive deposits on the pitting of regions of welded CS.
- Combining ML techniques showed that utilizing electrochemical data, environmental factors, and optimal CRW11 inhibitor dosages, the DT, RF, and XGBoost were the most viable ML models for this study with R^2 (99%). However, the least values of RMSE/MAE (0.2/0.2) of the RF model for welded CS without/with FeS deposit, while XGBoost performed best for welded CS, with FeS_2 deposit having the lowest RMSE/MAE (0.1/0.1). Hence, RF and XGBoost are appropriate to accurately predict the IE for welded CS without/with FeS and those with FeS_2, respectively.

This study enables a practical framework for managing PWC and pitting in welded CS pipelines under sour conditions as established by these findings. Although robust cross-validation and testing were employed, external validation on independent data sets would further establish model generalizability and is proposed for future work. In oil and gas systems, this paradigm makes it possible to choose materials more effectively, apply inhibitors more effectively, and control pipeline integrity better. All things considered, this study gives useful information for reducing the impact of PWC on vital oil and gas infrastructures while also advancing our understanding of PWC and pitting of welded CS in sour conditions.

■ ASSOCIATED CONTENT

Supporting Information

The Supporting Information is available free of charge at https://pubs.acs.org/doi/10.1021/acs.langmuir.5c02733.

LPR, Nyquist plots and summary of electrochemical results of welded CS regions without/with CRW11, summary of electrochemical results of welded CS regions with FeS deposit, without/with CRW11, summary of electrochemical results of welded CS regions with FeS_2 deposit, without/with CRW11, summary of weight loss corrosion test of CS-BM only, Raman spectra, surface compositions, SEM, elemental mapping and EDX of welded CS without/with CRW11, surface compositions, SEM, elemental mapping and EDX of CS-BM-FeS, CS-WM-FeS, CS-HAZ-FeS without/with CRW11, surface compositions, SEM, elemental mapping and EDX of CS-BM-FeS_2, CS-WM-FeS_2, CS-HAZ-FeS_2 without/with CRW11, microstructure images of pristine welded CS before and after corrosion without/with CRW11, summary of electrochemical parameters for 1D-artificial pit technique, optical microscope image of well-polished welded CS, and after ID pit tests for welded CS without/with FeS and FeS_2, and plots of ID artificial pit parameters: OCP, pitting kinetics, pit depth (calculated vs actual), aspect ratio, pit area and pit density (PDF)

■ AUTHOR INFORMATION

Corresponding Authors

Adewale K. Ipadeola − *Center for Advanced Materials, Qatar University, Doha, Qatar;* orcid.org/0000-0001-8896-6763; Email: ak.ipadeola@qu.edu.qa

Phaneendra K. Yalavarthy − *Department of Computational and Data Sciences (CDS), Indian Institute of Science (IISc), Bangalore 560012, India*; Email: yalavarthy@iisc.ac.in

Aboubakr M. Abdullah − *Center for Advanced Materials, Qatar University, Doha, Qatar;* orcid.org/0000-0001-8406-9782; Email: bakr@qu.edu.qa

Authors

Mostafa H. Sliem − *Center for Advanced Materials, Qatar University, Doha, Qatar*

Dana Abdeen − *Qatar Shell Research and Technology Centre, Doha, Qatar*

Nicholas Laycock − *Qatar Shell Research and Technology Centre, Doha, Qatar*

Ashwin RajKumar − *Department of Computational and Data Sciences (CDS), Indian Institute of Science (IISc), Bangalore 560012, India*

Complete contact information is available at: https://pubs.acs.org/10.1021/acs.langmuir.5c02733

Notes

The authors declare no competing financial interest.

■ ACKNOWLEDGMENTS

This work was financially supported by Academic Research Grant (ARG01-0524-230330) from the Qatar National Research Fund (QNRF) (a member of the Qatar Foundation).

All statements made herein are solely the responsibility of the authors. The authors would like to acknowledge the Qatar Shell Research and Technology Centre for financial support and access to laboratory facilities, and Central Laboratory Unit (CLU), Qatar University for SEM, EDX and elemental mapping.

REFERENCES

(1) Sabhapondit, A.; Abdullah, A. M.; Laycock, N.; Gonuguntla, M.; Madayi, S.; Bos, T. Inhibiting Localized Corrosion of Carbon Steel Pipelines in Sour Service. In *AMPP Annual Conference + Expo*; OnePetro, 2023; AMPP-2023-18833. Reda, A.; Shahin, M. A.; Montague, P. Review of Material Selection for Corrosion-Resistant Alloy Pipelines. *Eng. Sci.* **2025**, *33*, 1373. Pouranvari, M. Critical review on fusion welding of magnesium alloys: metallurgical challenges and opportunities. *Sci. Technol. Weld. Join.* **2021**, *26* (8), 559−580.

(2) Sun, J.; Tang, H.; Wang, C.; Han, Z.; Li, S. Effects of Alloying Elements and Microstructure on Stainless Steel Corrosion: A Review. *Steel Res. Int.* **2022**, *93*, 2100450. Niu, G.; Yuan, R.; Wang, E.; Yang, X.; Liu, Z.; Li, Z.; Zhang, Z.; Gong, N.; Li, K.; Su, B.; et al. Unraveling the influence of Mo on the corrosion mechanism of Ni-advanced weathering steel in harsh marine atmospheric environments. *J. Mater. Sci. Technol.* **2024**, *195*, 41−62. Li, Y.; Martín, D. S.; Wang, J.; Wang, C.; Xu, W. A review of the thermal stability of metastable austenite in steels: Martensite formation. *J. Mater. Sci. Technol.* **2021**, *91*, 200−214.

(3) Aljohani, T. A.; Alateyah, A. I.; El-Sanabary, S.; El-Garaihy, W. H. Chapter 16 - Corrosion of weldments. In *Welding of Metallic Materials*; Khoshnaw, F., Ed.; Elsevier, 2023; pp 565−588. Lahiri, A. K. Metallurgical Aspects of Welding. In *Applied Metallurgy and Corrosion Control: A Handbook for the Petrochemical Industry*; Springer Singapore, 2017; pp 141−176.

(4) Case, R.; Achour, M.; Daniels, J. Evaluation of Preferential Weld Corrosion Susceptibility and its Mitigation in Slightly Sour Conditions. In *Corrosion 2015*; NACE, 2015; NACE-2015−5640. Zhang, W. *Initiation and Propagation of Localized Corrosion of Mild Steel in Marginally Sour Environments*; Ohio University, 2020. https://etd.ohiolink.edu/acprod/odb_etd/etd/r/1501/10?clear=10&p10_accession_num=ohiou1605039352183903. Huggins Gonzalez, A. S. *Galvanic Interactions in Sweet and Sour Environments*. Ph.D., The Ohio State University: OH, USA, 2019. http://search.proquest.com.qulib.idm.oclc.org/dissertations-theses/galvanic-interactions-sweet-sour-environments/docview/2458759594/se-2.

(5) Choi, Y.-S.; Nešic, S.; Duan, D.; Jiang, S. Mechanistic Modeling of Carbon Steel Corrosion In a MDEA-Based CO2 Capture Process. In *Corrosion 2012*; NACE, **2012**.

(6) Rebak, R. B.; Perez, T. E. Effect of Carbon Dioxide and Hydrogen Sulfide on the Localized Corrosion of Carbon Steels and Corrosion Resistant Alloys. In *Corrosion 2017*; NACE, **2017**.

(7) Peng, S.; Rice John, D.; Zhang, W.; Luo, G.; Cao, H.; Pan, H. Laboratory Investigation of the Effects of Blanket Defect Size on Initiation of Backward Erosion Piping. *J. Geotech. Geoenviron.* **2024**, *150* (10), 04024095.

(8) Wang, X.; Yong, Y.; Chen, Y.; Wang, H.; Wei, K. Corrosion Behavior of X100 Pipeline Steel and Its Heat-Affected Zones in Simulated Alkaline Soil Solution. *Int. J. Electrochem. Sci.* **2019**, *14* (9), 9181−9192.

(9) Jun, J.; Unocic, K.; Petrova, M.; Shipilov, S. A.; Carvalhaes, T.; Thakur, G. M.; Piburn, J.; Pint, B. *Methodologies for Evaluation of Corrosion Protection for Ductile Iron Pipe; ORNL/TM-2017/144*; Oak Ridge National Laboratory (ORNL): Oak Ridge, TN, 2019. Tang, K.; Hong, T. Z. X.; You, L.; Zhou, K. Carbon−metal compound composite electrodes for capacitive deionization: synthesis, development and applications. *J. Mater. Chem. A* **2019**, *7* (47), 26693−26743. Abdullah, A. M.; Fayyad, E. M.; Ipadeola, A. K.; Sliem, M. H.; Abdeen, D.; Al-Qahtani, N.; RajKumar, A.; Jeffrey, J.; Yalavarthy, P. Electrochemical and machine learning analysis unveils protective mechanisms of commercial amine-based inhibitors for under-deposit corrosion of carbon steel in sour media. In *248th Electrochemical Society (ECS) Meeting*; ECS, 2025. https://ecs.confex.com/ecs/248/meetingapp.cgi/Paper/207747.

(10) Turris, A. D.; Romero, M. F. d.; Papavinasam, S. Corrosive aggressiveness of water production due to the SRB and CO2. *Rev. Téc. Ing. Univ. Zulia.* **2016**, *39*, 397−403.

(11) Liu, C.; Du, P.; Zhao, H.; Wang, L. Synthesis of l-Histidine-Attached Graphene Nanomaterials and Their Application for Steel Protection. *ACS Applied Nano Mater.* **2018**, *1* (3), 1385−1395.

(12) Quraishi, M. A.; Chauhan, D. S.; Ansari, F. A. Development of environmentally benign corrosion inhibitors for organic acid environments for oil-gas industry. *J. Mol. Liq.* **2021**, *329*, 115514.

(13) Thabet, H. K.; El-Shamy, O. A. A.; Ashmawy, A. M.; Deyab, M. A. The Impact of Corrosion Inhibitors in Desalination Systems. *ACS Omega* **2023**, *8* (48), 45224−45231.

(14) Dagdag, O.; Safi, Z.; Hsissou, R.; Erramli, H.; El Bouchti, M.; Wazzan, N.; Guo, L.; Verma, C.; Ebenso, E. E.; El Harfi, A. Epoxy pre-polymers as new and effective materials for corrosion inhibition of carbon steel in acidic medium: Computational and experimental studies. *Sci. Rep.* **2019**, *9* (1), 11715. Nwanonenyi, S. C.; Obasi, H. C.; Chukwujike, I. C.; Chidiebere, M. A.; Oguzie, E. E. Inhibition of Carbon Steel Corrosion in 1 M H2SO4 Using Soy Polymer and Polyvinylpyrrolidone. *Chem. Afr.* **2019**, *2* (2), 277−289. Jawad, Q. A.; Zinad, D. S.; Dawood Salim, R.; Al-Amiery, A. A.; Sumer Gaaz, T.; Takriff, M. S.; Kadhum, A. A. H. Synthesis, Characterization, and Corrosion Inhibition Potential of Novel Thiosemicarbazone on Mild Steel in Sulfuric Acid Environment. *Coatings* **2019**, *9* (11), 729. Fayyad, E. M.; Ipadeola, A. K.; Sliem, M. H.; Abdeen, D.; Al-Qahtani, N.; RajKumar, A.; Jeffrey, J.; Yalavarthy, P.; Abdullah, A. M. Interfacial robustness of commercial amine-based inhibitors mitigates under-deposit corrosion of carbon steel in simulated sour conditions: A merged electrochemical and machine learning study. *Emergent Mater.* **2025**, 4.

(15) Kvryan, A.; Efaw, C. M.; Higginbotham, K. A.; Maryon, O. O.; Davis, P. H.; Graugnard, E.; Trivedi, H. K.; Hurley, M. F. Corrosion Initiation and Propagation on Carburized Martensitic Stainless Steel Surfaces Studied via Advanced Scanning Probe Microscopy. *Materials* **2019**, *12* (6), 940. McMurtrey, M. D.; Mills, D. E.; Burns, J. T. The effect of pit size and density on the fatigue behaviour of a pre-corroded martensitic stainless steel. *Fatigue Fract. Eng. Mater. Struct.* **2019**, *42* (1), 3−18. Luo, S.; Liu, M.; Wen, N.; Shen, Y.; Liu, Y.; Lin, X. Effect of pre−corrosion on Electrochemical Corrosion and Fatigue Behavior of S135 High−Strength Drill Pipe Steel in Marine Environment. *Int. J. Electrochem. Sci.* **2019**, *14* (3), 2589−2605. Joseline, D.; Pillai, R. G. Electrochemical/Microstructural Studies on the Corrosion of Prestressed Steel Strand in Concrete with Naturally Ingressing Chlorides. *Corrosion* **2022**, *78* (11), 1126−1142. Li, J.; Hughes, A. E.; Yang, Y. S.; Laleh, M.; Wang, H.; Zhang, X.; Ma, J.; Xu, W.; Tan, M. Y. Quantitative 3D Characterization for Kinetics of Corrosion Initiation and Propagation in Additively Manufactured Austenitic Stainless Steel. *Adv. Sci.* **2022**, *9* (36), 2201162. Zhang, H.; Liu, H.; Deng, Y.; Cao, Y.; He, Y.; Liu, Y.; Deng, Y. Fatigue behavior of high-strength steel wires considering coupled effect of multiple corrosion-pitting. *Corros. Sci.* **2025**, *244*, 112633.

(16) Guan, X.; Enalls, B. C.; Clarke, D. R.; Girguis, P. Iron Sulfide Formation on Iron Substrates by Electrochemical Reaction in Anoxic Conditions. *Cryst. Growth Des.* **2017**, *17* (12), 6332−6340.

(17) Alabtah, F. G.; Alkhouzaam, A.; Eliyan, F. F.; Ansari, N.; Alhamidi, Y.; Khraisheh, M. Advancing the industrial utilization of additive manufacturing: Understanding early-stage corrosion dynamics through advanced electrochemical and microstructural characterization. *J. Mater. Res. Technol.* **2025**, *35*, 2525−2546. Wang, W.; Mu, W.; Han, M.; Zhang, Y.; Wang, N.; Zhang, W.; Li, Z.; Weng, Z.; Liaw, P. K. An integration study of corrosion and mechanical behaviors of Ti-/Zr-/Hf-doped cobalt-based high-entropy alloys. *Materdes* **2025**, *256*, 114230.

https://doi.org/10.1021/acs.langmuir.5c02733
Langmuir 2025, 41, 23632−23651

(18) Nyby, C.; Guo, X.; Saal, J. E.; Chien, S.-C.; Gerard, A. Y.; Ke, H.; Li, T.; Lu, P.; Oberdorfer, C.; Sahu, S.; et al. Electrochemical metrics for corrosion resistant alloys. *Sci. Data* **2021**, *8* (1), 58.
(19) Adasooriya, N. D.; Samarakoon, S. M. K.; Gudmestad, O. T. Corrosion Propagation Phase And Bond Strength Degradation Of Reinforced Concrete Structures: State Of The Art. *Int. J. Comput. Methods Exp. Meas.* **2018**, *6*, 499−514. Li, Y.; Wang, Q.; Zhu, W.; Ding, S.; Xing, L.; Bai, Z.; Wang, Y. Corrosion characteristics and mechanisms of ceramic coatings in subcritical and supercritical aqueous systems. *Ceram. Int.* **2025**, *51* (15), 19743−19760.
(20) Coelho, L. B.; Zhang, D.; Van Ingelgem, Y.; Steckelmacher, D.; Nowé, A.; Terryn, H. Reviewing machine learning of corrosion prediction in a data-oriented perspective. *npj Mater. Degrad.* **2022**, *6* (1), 8.
(21) Ruiz, D.; Casas, A.; Escobar, C. A.; Perez, A.; Gonzalez, V. Advanced Machine Learning Techniques for Corrosion Rate Estimation and Prediction in Industrial Cooling Water Pipelines. *Sensors* **2024**, *24* (11), 3564. Meng, X.; Zhuang, W.; Lin, L.; Li, H.; Cao, Z.; Mei, H. Characteristics of streamer discharge in SF6 gas under different pressures. *IEEE Trans. Dielectr. Electr. Ins.* **2025**, *32*, 1583−1590. Mallieswaran, K.; Padmanabhan, R.; Balasubramanian, V. Friction stir welding parameters optimization for tailored welded blank sheets of AA1100 with AA6061 dissimilar alloy using response surface methodology. *Adv. Mater. Process. Te.* **2018**, *4* (1), 142−157.
(22) Dong, Z.; Ding, L.; Meng, Z.; Xu, K.; Mao, Y.; Chen, X.; Ye, H.; Poursaee, A. Machine learning-based corrosion rate prediction of steel embedded in soil. *Sci. Rep.* **2024**, *14* (1), 18194.
(23) Dong, Z.; Zhang, M.; Li, W.; Wen, F.; Dong, G.; Zou, L.; Zhang, Y. Development of a Predictive Model for Carbon Dioxide Corrosion Rate and Severity Based on Machine Learning Algorithms. *Materials* **2024**, *17* (16), 4046.
(24) Narku-Tetteh, J.; Mensah, E.; Muchan, P.; Supap, T.; Lisawadi, S.; Idem, R. Development of experimental error-Driven model for prediction of corrosion rates of amines based on their chemical structures. *Heliyon* **2023**, *9* (11), e22050.
(25) Lee, J.; Kumar, S.; Lee, S.-Y.; Park, S. J.; Kim, M.-h. Development of Predictive Models for Identifying Potential S100A9 Inhibitors Based on Machine Learning Methods. *Front. Chem.* **2019**, *7*, 779.
(26) Meng, X.; Zhang, B.; Cao, F.; Liao, Y. Coupling Effect Between HVDC Grounding Electrode and Natural Gas Pipelines Considering Complex Soil Structure Model. *IEEE Trans. Power Delivery* **2025**, *40*, 2040−2047.
(27) Kermani, M. B.; Morshed, A. Carbon Dioxide Corrosion in Oil and Gas Production—A Compendium. *Corrosion* **2003**, *59* (8), 659−683.
(28) Lan, L.; Kong, X.; Chang, Z.; Qiu, C.; Zhao, D. Microstructure, Composition, and Impact Toughness Across the Fusion Line of High-Strength Bainitic Steel Weldments. *Metall. Mater. Trans. A Phys. Metall. Mater. Sci.* **2017**, *48* (9), 4140−4153.
(29) Ren, D.; Wang, C.; Wei, X.; Zhang, Y.; Han, S.; Xu, W. Harmonizing physical and deep learning modeling: A computationally efficient and interpretable approach for property prediction. *Scripta Materialia* **2025**, *255*, 116350.
(30) Park, J. S.; Lee, J. W.; Kim, S. J. Hydrogen-induced cracking caused by galvanic corrosion of steel weld in a sour environment. *Materials* **2021**, *14* (18), 5282.
(31) Yang, L.; Ma, Z.; Zheng, Y.; Wang, X.; Huang, Y.; Wang, K.; Song, S.; Jin, W. The Study of Corrosion Behaviors of Carbon Steel Weldments and Their Inhibition in Simulated Pore Solution Using Multi-Electrode Array Technique. *Appl. Sci.* **2021**, *11* (18), 8278.
(32) Munir, S.; Pelletier, M. H.; Walsh, W. R. Potentiodynamic corrosion testing. *J. Vis. Exp.* **2016**, *115*, 54351.
(33) Palumbo, G.; Dunikowski, D.; Wirecka, R.; Mazur, T.; Lelek-Borkowska, U.; Wawer, K.; Banaś, J. Effect of grain size on the corrosion behavior of Fe-3wt.% Si-1wt.% Al electrical steels in pure water saturated with CO2. *Materials* **2021**, *14* (17), 5084. Kolli, S.; Javaheri, V.; Kömi, J.; Porter, D. On the role of grain size and carbon content on the sensitization and desensitization behavior of 301 austenitic stainless steel. *Metals* **2019**, *9* (11), 1193.
(34) Al-Amiery, A. A.; Isahak, W. N. R. W.; Al-Azzawi, W. K. Corrosion inhibitors: natural and synthetic organic inhibitors. *Lubricants* **2023**, *11* (4), 174.
(35) Salah, B.; Ipadeola, A. K.; Abdullah, A. M.; Ghanem, A.; Eid, K. Self-Standing Pd-Based Nanostructures for Electrocatalytic CO Oxidation: Do Nanocatalyst Shape and Electrolyte pH Matter? *Int. J. Mol. Sci.* **2023**, *24* (14), 11832. Ipadeola, A. K.; Salah, B.; Ghanem, A.; Ahmadaliev, D.; Sharaf, M. A.; Abdullah, A. M.; Eid, K. Unveiling the effect of shapes and electrolytes on the electrocatalytic ethanol oxidation activity of self-standing Pd nanostructures. *Heliyon* **2023**, *9* (6), e16890. Airo, M. A.; Otieno, F.; Mxakaza, L.; Ipadeola, A.; Kadzutu-Sithole, R. S.; Machogo-Phao, L. F.; Billing, C.; Moloto, M.; Moloto, N. Probing the stoichiometry dependent catalytic activity of nickel selenide counter electrodes in the redox reaction of iodide/triiodide electrolyte in dye sensitized solar cells. *RSC Adv.* **2020**, *10* (65), 39509−39520.
(36) Shi, Z.; Fang, C.; Li, J.; Bandaru, S.; Liu, M.; Zhao, L.; Zhang, X. Multi-Dimensional Design of Slippery Liquid-Infused Coatings Empowering Long-Term Corrosion Protection for Sintered Nd-Fe-B Magnets in Harsh Environments. *Small* **2025**, *21* (22), 2500629.
(37) Ribeiro, D. V.; Souza, C. A. C.; Abrantes, J. C. C. Use of Electrochemical Impedance Spectroscopy (EIS) to monitoring the corrosion of reinforced concrete. *Rev. IBRACON Estrut. Mater.* **2015**, *8* (4), 529−546.
(38) Ariyoshi, K.; Siroma, Z.; Mineshige, A.; Takeno, M.; Fukutsuka, T.; Abe, T.; Uchida, S. Electrochemical Impedance Spectroscopy Part 1: Fundamentals. *Electrochemistry* **2022**, *90* (10), 102007.
(39) Laschuk, N. O.; Easton, E. B.; Zenkina, O. V. Reducing the resistance for the use of electrochemical impedance spectroscopy analysis in materials chemistry. *RSC Adv.* **2021**, *11* (45), 27925−27936.
(40) Bleij, A.; Ponomareva, M.; Nadlinger, M.; Schimo-Aichhorn, G.; Bingemann, D.; Rathmell, C.; Luckeneder, G.; Haslehner, G.; Gattinger, P.; Brandstetter, M.; Bilotto, P.; Valtiner, M. In situ Raman Spectroscopy Monitors the Corrosion of Mild Steel in a Salt Fog Chamber. *Spectrosc. Suppl.* **2022**, *37* (s6), 8−18.
(41) Surnam, B. Y. R.; Chui, C.-W.; Xiao, H.; Liang, H. Investigating atmospheric corrosion behavior of carbon steel in coastal regions of Mauritius using Raman Spectroscopy. *Matéria (Rio J.)* **2016**, *21* (1), 157−168.
(42) Heuer, J.; Luttge, A. Kinetics of pipeline steel corrosion studied by Raman spectroscopy-coupled vertical scanning interferometry. *Npj Mater. degrad.* **2018**, *2* (1), 40.
(43) Santa, A. C.; Montoya, D. A.; Tamayo, J. A.; Gómez, M. A.; Castaño, J. G.; Baena, L. M. Atmospheric corrosion of carbon steel: Results of one-year exposure in an andean tropical atmosphere in Colombia. *Heliyon* **2024**, *10* (8), e29391.
(44) Li, B.; Xia, Q.; Dong, W. Comparative Study of the Corrosive Behaviors of Rust Layers on Bronze Ware in Different Corrosive Environments. *Materials* **2025**, *18* (6), 1359. Natesan, M.; Selvaraj, S.; Manickam, T.; Venkatachari, G. Corrosion behavior of metals and alloys in marine-industrial environment. *Sci. Technol. Adv. Mater.* **2008**, *9* (4), 045002.
(45) Fakheri, M.; Zare, H. R.; Mohammadpour, Z.; Mosallaee, M. The impact of Ni on the corrosion behavior and microstructure of weld metal fabricated from E8018-G electrodes. *Weld. World.* **2020**, *64* (6), 1065−1075.
(46) Katiyar, P. K.; Maurya, R.; Singh, P. K. Highlighting the corrosion mechanisms of corroded plain carbon steels using the atomic force microscopy. *Int. J. Sustain. Build. Technol. Urban Dev.* **2022**, *13* (2), 198−220.
(47) Zhang, Z.; Studer, P.; Angst, U. A multi-technique study of corrosion products at the steel-concrete interface under two exposure conditions. *J. Microsc.* **2022**, *286* (2), 191−197.
(48) Alawadhi, K. A.; Robinson, M. J. Preferential weld corrosion of X65 pipeline steel in flowing brines containing carbon dioxide. *Corros. Eng. Sci. Technol.* **2011**, *46* (4), 318−329. (b) Choi, Y. Y.; Kim, M. H.

https://doi.org/10.1021/acs.langmuir.5c02733
Langmuir 2025, 41, 23632−23651

Corrosion behaviour of welded low-carbon steel in the Arctic marine environment. *RSC Adv.* **2018**, *8* (53), 30155−30162.
(49) Branzoi, F.; Branzoi, V.; Licu, C. Corrosion inhibition of carbon steel in cooling water systems by new organic polymers as green inhibitors. *Mater. Corros.* **2014**, *65* (6), 637−647.
(50) Sherar, B. W. A.; Keech, P. G.; Shoesmith, D. W. The effect of aerobic corrosion on anaerobically-formed sulfide layers on carbon steel in dilute near-neutral pH saline solutions. *Corros. Sci.* **2013**, *77*, 257−264. Kato, N.; Yamada, M.; Ojima, J.; Takaya, M. Analytical method using SEM-EDS for metal elements present in particulate matter generated from stainless steel flux-cored arc welding process. *J. Hazard Mater.* **2022**, *424* (Pt B), 127412.
(51) Diaz-Mateus, M. A.; Salgar-Chaparro, S. J.; Machuca, L. L.; Farhat, H. Effect of deposit chemistry on microbial community structure and activity: Implications for under-deposit microbial corrosion. *Front. Microbiol.* **2023**, *14*, 1089649.
(52) Chan, W. M. M. *A critical study on corrosion and corrosion control methods for piping systems in Hong Kong*; Hong Kong Polytechnic University: Hong Kong, 2003.
(53) Qu, X.; Li, X.; Zhang, L.; Yi, D.; Wang, J.; Wen, C.; Zhao, Z.; Gu, X.; Lin, Y.; Liu, B.; et al. Effect of construction angles on the microstructure and mechanical properties of LPBF-fabricated 15−5 PH stainless steel. *Mater. Sci. Eng., A* **2024**, *900*, 146423. Long, Z.; Yongliang, H.; Xuemei, D.; Xin, L.; Limeng, Y.; Yuhua, C.; Jilin, X. Formation mechanism of waveform interface in Mg/Al electromagnetic pulse welding. *Mater. Today Commun.* **2025**, *45*, 112401. Zhang, X.; Xue, K.; Liu, L.; Xiao, J.; Liu, J.; Jin, F.; Luo, M.; Zhan, M.; Li, H. Effect of electrical pulse treatment on the microstructural and mechanical responses of heterogeneous linear friction welded TC17/TC4 dissimilar joint. *J. Mater. Res. Technol.* **2025**, *35*, 1−12.
(54) Rajesh, A.; Karthick, S.; Mallieswaran, K.; Shanmugam, R. *Tensile strength analysis of electron beam welded AA2024 aluminum alloy joints*; SAE Technical Paper, 2024. Mallieswaran, K.; Agaramudhalvan, S.; George Oliver, D. Microstructural stability and strength correlation in AGG-affected friction stir welded AA2024-T4 joints. *Adv. Mater. Process. Te.* **2025**, 1−10. Rajendran, C.; Ben Ruben, R.; Ashokavarthanan, P.; Mallieswaran, K. Identifying the effect of PWHT on strength of laser beam welding joints of AA2024 aluminum alloy. *ASME Open J. Eng.* **2022**, *1*, 011003.
(55) Song, L.; Peng, Y.; Zhao, H.; Cao, Y.; Fang, Q. Corrosion resistance analysis of the weld metal of low-alloy high-strength steel considering different alloy compositions. *Front. Mater.* **2022**, *9*, 957669. Orhorhoro, E. K.; Erameh, A. A.; Tamuno, R. I. Investigation of the effect of corrosion rate on post welded heat treatment of medium carbon steel in seawater. *J. Appl. Res. Ind. Eng.* **2022**, *9* (1), 59−67.
(56) Zhang, S.; Zhao, H.; Shu, F.; He, W.; Wang, G. Microstructure and corrosion behavior of simulated welding HAZ of Q315NS steel in sulfuric acid solution. *Metals* **2017**, *7* (6), 194.
(57) Kuppusamy, M.; Rajendran, S.; Baruch, L. J. Strength Analysis of CMT and Pulsed CMT Welded AA8011 Aluminum Alloy Joints. In *Advances in Solid-State Welding and Processing of Metallic Materials*, 1st edition; CRC Press, 2025; pp 195−204.
(58) Ko, S.-J.; An, J.-H.; Kim, Y.-S.; Kim, W.-C.; Kim, J.-G. Effects of corrosion on mechanical properties of welded carbon steel pipe in district heating water. *Materials* **2019**, *12* (22), 3682.
(59) Dong, Y.; Liu, D.; Du, H.; Sun, H.; Zuo, X. Effect of microstructure on the mechanical properties and corrosion resistance of a welded joint of 620-grade marine steel. *Front. Mater.* **2023**, *10*, 1107125.
(60) Liu, J.; Wang, B.; Chen, T.; Hao, L.; Wu, J.; Liu, C. The Effect of Corrosion Inhibitors on the Corrosion Behavior of Ductile Cast Iron. *Metals* **2025**, *15* (1), 70. Chen, L.; Lu, D.; Zhang, Y. Organic compounds as corrosion inhibitors for carbon steel in HCl solution: a comprehensive review. *Materials* **2022**, *15* (6), 2023.
(61) Liu, H.; Fu, C.; Gu, T.; Zhang, G.; Lv, Y.; Wang, H.; Liu, H. Corrosion behavior of carbon steel in the presence of sulfate reducing bacteria and iron oxidizing bacteria cultured in oilfield produced water. *Corros. Sci.* **2015**, *100*, 484−495.
(62) Avci, R.; Davis, B. H.; Rieders, N.; Lucas, K.; Nandasiri, M.; Mogk, D. Role of metallurgy in the localized corrosion of carbon steel. *J. Miner. Mater. Charact. Eng.* **2018**, *6* (6), 618−646.
(63) Sridhar, G. *Failure analysis of free-cutting grade steels: a case study*; NML, 1997; pp 121−139.
(64) Setti, N.; Barrahi, A.; Maatallah, M.; Kaddouri, Y.; Hadda, T. B.; Outada, H.; Thakur, A.; Touzani, R.; Karrouchi, K.; Abuelizz, H. A.; Dikici, B.; Zarrouk, A.; Dafali, A. Experimental and computational approach on the corrosion inhibition properties of two newly pyrazole derivatives on carbon steel in acid medium. *Sci. Rep.* **2025**, *15* (1), 3631.
(65) Liu, H.; Meng, G.; Li, W.; Gu, T.; Liu, H. Microbiologically influenced corrosion of carbon steel beneath a deposit in CO2-saturated formation water containing Desulfotomaculum nigrificans. *Front. Microbiol.* **2019**, *10*, 1298.
(66) Shen, Z.; Dohr, J.; Lozano-Perez, S. The effects of intergranular carbides on the grain boundary oxidation and cracking in a cold-worked Alloy 600. *Corros. Sci.* **2019**, *155*, 209−216. Blancas-Garcia, V.; Garcia, E.; Garcia, C. I. A new view of the grain-coarsening behavior of austenite and the role of high-mobility boundaries in ti-microalloyed low-carbon steels. *Mater. Sci. Technol.* **2017**, 1030−1037.
(67) Butler, K. T.; Davies, D. W.; Cartwright, H.; Isayev, O.; Walsh, A. Machine learning for molecular and materials science. *Nature* **2018**, *559* (7715), 547−555. Diao, Y.; Yan, L.; Gao, K. Improvement of the machine learning-based corrosion rate prediction model through the optimization of input features. *Mater. Des.* **2021**, *198*, 109326.
(68) Chen, T.; Guestrin, C. Xgboost: A scalable tree boosting system. In *Proceedings of the 22nd acm sigkdd international conference on knowledge discovery and data mining*; ACM, 2016; pp 785−794.

https://doi.org/10.1021/acs.langmuir.5c02733
Langmuir 2025, 41, 23632−23651